

Green-function theory of confined plasmons in coaxial cylindrical geometries: Zero magnetic fieldM. S. Kushwaha¹ and B. Djafari-Rouhani²¹*Institute of Industrial Science, University of Tokyo, 4-6-1 Komaba, Meguro-Ku, Tokyo 153-8505, Japan*²*UFR de Physique, CNRS 8024, University of Science and Technology of Lille I, 59655 Villeneuve d'Ascq Cedex, France*

(Received 9 January 2003; revised manuscript received 10 March 2003; published 26 June 2003)

A theoretical investigation is made of the plasmon propagation in the coaxial cylindrical geometries using Green function (or response function) theory in the absence of an applied magnetic field. The plasmon excitations in such multiple interface structures are characterized by the electromagnetic (EM) fields that are localized at and decay exponentially away from the interfaces. The Green-function theory, generalized to be applicable to such quasi-one-dimensional (1D) systems, enables us to derive explicit expressions for the corresponding response functions (associated with EM fields), which can in turn be used to compute numerous physical properties of the system at hand. A rigorous analytical diagnosis of the general results in diverse situations leads us to reproduce exactly the previously well-established results on 2D and 1D systems, obtained within the different theoretical frameworks. As an application, we present several illustrative examples on the dispersion characteristics of the confined and extended plasmons in single- and double-interface structures. These dispersive modes are also substantiated through the computation of local as well as total density of states. Our theoretical framework can also serve as a powerful technique for studying the intrasubband plasmons in the emerging multiple-walled carbon nanotubes. The elegance of theory lies in the fact that it does not require the matching of the messy boundary conditions and in its simplicity and the compact form of the desired results.

DOI: 10.1103/PhysRevB.67.245320

PACS number(s): 52.35.Hr, 68.65.La, 78.67.Ch

I. INTRODUCTION

The past two decades have seen a great deal of research efforts focused on semiconducting systems of reduced dimensions and size. The ability to make progressively smaller structures has allowed researchers to study how the charge carriers behave when confined to still lower dimensions. Thus the advancement of research on electronic systems has been predominantly toward more confinement—from quantum well (two degrees of freedom) to quantum wire (one degree of freedom) to quantum dots (zero degree of freedom). The basic principle behind the growth mechanism of quantum wells, wires, and dots is the same: confine electrons in a restricted region of a semiconductor by sandwiching it within another semiconductor with a larger band gap, a measure of the amount of energy needed to get the electrons flowing. Theoretically, the reduced degrees of freedom allow detailed and often exact calculations. Practically, new and exotic electronic and optical phenomena have been observed. An extensive recent review of the subject, both theoretical and experimental, can be found in Ref. 1.

The current status of the nanofabrication technology leads us to imagine formation of not only two-dimensional (2D), 1D, and 0D structures, but also more complicated ones such as quantum pipes, snakes, balls, rings, and ribbons where electrons are confined in the regions with quasi-dimensionality between three and zero dimensions (see Ref. 1). The fabrication of essentially arbitrary geometries could lead to dramatic control of the electronic and optical properties of solids. Role of the boundaries—the inner and outer perimeters—in understanding several electronic and transport phenomena in such nanostructures has been much appreciated in the recent past. We refer, in particular, to the importance of the edge states in understanding, for example,

the magnetotransport in quantum Hall regimes in a broad range of mesoscopic systems.¹ In this context, Foden *et al.*² have reported results on the band structure and conductance of axially symmetric, curved, non-interacting 2D electron gas (2DEG), topologically equivalent to a Corbino disk, in the presence of non-homogeneous magnetic field, arising as a result of an applied axial magnetic field.

The optical phenomena being investigated within the classical electrodynamics continues to receive a considerable attention on the nanoscale cylindrical as well as spherical structures. The cylindrical structures have generated particular interest for their usefulness not just as electromagnetic waveguides, but also as atom guides, where the guiding mechanism is governed mainly by the excited cavity modes. It is envisioned that the understanding of atom guides at such a small scale would lead to much desirable advancements in atom lithography, which in turn should facilitate the atomic physics research.³

The present work is aimed at investigating the plasma modes of a semiconductor (dielectric) shell embedded in the two unidentical dielectrics (semiconductors) in the coaxial cylindrical geometries using a Green-function theory in the absence of an applied magnetic field. Our theoretical approach is virtually the interface response theory (IRT) (Ref. 4) generalized to be applicable to such quasi-one-dimensional systems. Ever since its inception, the IRT has been extensively applied to study various quasi-particle excitations (such as phonons, plasmons, magnons, etc.) in heterostructures and superlattices.^{5–7} Quite recently, it was generalized to investigate diverse 2D systems, both with and without an applied magnetic field.^{8,9}

Such semiclassical theories (including the hydrodynamical model which can also accommodate the spatial dispersion in a simple manner) and the quantal theories such as

Bohm-Pines' random-phase approximation¹⁰ are supposed to produce identical results for the intrasubband collective excitations for the corresponding quantum systems in the long-wavelength limit. In the limit that both radii of the inner and outer cylinders R_1 and $R_2 \rightarrow \infty$ but $d = (R_2 - R_1)$ remains a finite quantity, we will show how we obtain exactly the dispersion relation for the intrasubband plasmons in an inversion-layer system, which represents the 2D geometries. Similarly, in the limit that the radius of a plasma cylinder $R \rightarrow 0$, our theoretical results are shown to yield the dispersion relation for the intrasubband plasmons for a single quantum wire.

The general results on the confined as well as extended plasma modes, in both single and double-interface geometries, are shown to be correctly substantiated by the local and/or total density of states. Apart from such tests of the theory, we believe that it should prove to be a simple but powerful scheme of a theoretical framework needed to study, for example, the intrasubband plasmons in multiwalled carbon nanotubes, where theoretical research is gaining considerable momentum recently.¹¹

The rest of the paper is organized as follows. In Sec. II we discuss some basic notions of the cylindrical geometry and calculate the bulk response function. In Sec. III we present a theoretical formalism to derive the final expressions for the plasmon dispersion relations, discuss some interesting analytical diagnosis of the general expressions under special limits, and give some explicit analytical relationship between the response functions and the density of states. In Sec. IV we report several illustrative examples of the numerical results on the plasmon dispersion and density of states in a variety of experimentally feasible situations. Finally, in Sec. V we conclude our findings and list some interesting dimensions worth adding to the problem in the future.

II. BASIC NOTIONS AND BULK RESPONSE FUNCTIONS

First we consider it important to make a careful analysis of the Maxwell equations before making their use for deriving the response functions for the respective systems. We consider the electromagnetic waves propagating with an angular frequency ω and wave vector $k \parallel \hat{z}$ in a medium defined by the cylindrical coordinates (ρ, θ, z) . The plasma waves, here as well as in the later part of this work, will be assumed to observe a spatial localization along the direction perpendicular to the axis of the cylinder. Note that the situation is totally unlike that in the Cartesian coordinate system where one can safely and readily define the sagittal plane (i.e., the plane defined by the wave vector and the normal to the surface/interface) and hence isolate the transverse magnetic (TM) and the transverse electric (TE) modes, at least in the absence of an applied magnetic field. The only exception to this notion is the Voigt geometry (with a magnetic field parallel to the surface/interface and perpendicular to the propagation vector) that can still (i.e., even in the presence of an applied magnetic field) allow the separation of the TM and TE modes (see, for details, Ref. 1). In the literature on optics the TM and TE modes are also known by the name of p and s polarizations, respectively.

It should be pointed out that we are interested in the non-magnetic materials, so that $\vec{B} \equiv \vec{H}$ in the Maxwell curl-field equations. After eliminating the magnetic field variable \vec{B} from these curl-field equations, we obtain

$$\vec{\nabla} \times (\vec{\nabla} \times \vec{E}) - q_0^2 \epsilon \vec{E} = 0. \quad (2.1)$$

Here the dielectric constant ϵ is a scalar quantity, since the system we are concerned with is not subjected to any external magnetic field and the physical system is assumed to be isotropic. In Eq. (2.1) $q_0 = \omega/c$ is the vacuum wave vector, where c is the speed of light in vacuum. We will take the spatial and temporal dependence of the electromagnetic fields of the form of $\vec{A}(\rho, \phi, z) \sim \vec{A}(\rho, \theta) e^{(ikz - i\omega t)}$, where $\vec{A} \equiv \vec{E}$ or \vec{B} . Recalling the standard definitions of $\vec{\nabla} \cdot \vec{A}$, $\nabla^2 \phi$ (with ϕ as any scalar), and $\vec{\nabla} \times \vec{A}$ in the cylindrical coordinates, one should be able to split Eq. (2.1) into the three equations:

$$\left[\frac{\partial^2}{\partial \rho^2} + \frac{1}{\rho} \frac{\partial}{\partial \rho} + \frac{1}{\rho^2} \frac{\partial^2}{\partial \theta^2} - k^2 \right] E_x - \frac{1}{\rho^2} \left(E_x + 2 \frac{\partial}{\partial \theta} E_y \right) + q_0^2 \epsilon E_x = 0, \quad (2.2)$$

$$\left[\frac{\partial^2}{\partial \rho^2} + \frac{1}{\rho} \frac{\partial}{\partial \rho} + \frac{1}{\rho^2} \frac{\partial^2}{\partial \theta^2} - k^2 \right] E_y - \frac{1}{\rho^2} \left(E_y - 2 \frac{\partial}{\partial \theta} E_x \right) + q_0^2 \epsilon E_y = 0, \quad (2.3)$$

$$\left[\frac{\partial^2}{\partial \rho^2} + \frac{1}{\rho} \frac{\partial}{\partial \rho} + \frac{1}{\rho^2} \frac{\partial^2}{\partial \theta^2} - k^2 \right] E_z + q_0^2 \epsilon E_z = 0. \quad (2.4)$$

Equations (2.2)–(2.4) demonstrate clearly that the cylindrical geometry does not allow the separation of the TM and TE modes. We choose to work in terms of E_z and B_z components. Then we first need to evaluate E_x , E_y , B_x , and B_y in terms of E_z and B_z from the Maxwell curl-field equations. The results are

$$E_x = \frac{1}{\alpha^2} \left[-iq_0 \frac{1}{\rho} \frac{\partial}{\partial \theta} B_z - ik \frac{\partial}{\partial \rho} E_z \right], \quad (2.5)$$

$$E_y = \frac{1}{\alpha^2} \left[iq_0 \frac{\partial}{\partial \rho} B_z - ik \frac{1}{\rho} \frac{\partial}{\partial \theta} E_z \right], \quad (2.6)$$

and similarly

$$B_x = \frac{1}{\alpha^2} \left[iq_0 \epsilon \frac{1}{\rho} \frac{\partial}{\partial \theta} E_z - ik \frac{\partial}{\partial \rho} B_z \right], \quad (2.7)$$

$$B_y = \frac{1}{\alpha^2} \left[-iq_0 \epsilon \frac{\partial}{\partial \rho} E_z - ik \frac{1}{\rho} \frac{\partial}{\partial \theta} B_z \right]. \quad (2.8)$$

With the aid of these equations, we simplify the z components of the Maxwell curl-field equations:

$$\frac{1}{\rho} \frac{\partial}{\partial \rho} (\rho E_y) - \frac{1}{\rho} \frac{\partial}{\partial \theta} E_x = i q_0 B_z \quad (2.9)$$

and

$$\frac{1}{\rho} \frac{\partial}{\partial \rho} (\rho B_y) - \frac{1}{\rho} \frac{\partial}{\partial \theta} B_x = -i q_0 \epsilon E_z, \quad (2.10)$$

to write

$$\frac{\partial^2}{\partial \rho^2} A_z + \frac{1}{\rho} \frac{\partial}{\partial \rho} A_z + \left(\frac{1}{\rho^2} \frac{\partial^2}{\partial \theta^2} - \alpha^2 \right) A_z = 0, \quad (2.11)$$

where A_z stands for E_z or B_z and $\alpha = (k^2 - q_0^2 \epsilon)^{1/2}$ is a measure of the decay constant in a medium concerned.

Before we proceed further, it is important to define a characteristic terminology of the interface response theory: the black-box surface (BBS). By the BBS we mean an entirely opaque surface through which electromagnetic fields cannot propagate. The idea of introducing the BBS in the IRT (Ref. 4) was conceived with two prominent advantages over the contemporary semiclassical approaches in mind. First, it allows one to disconnect from the extra mathematical world and hence to confine only within the truly building block of the system concerned. Second, it implicitly provides a great opportunity to get rid of using the messy boundary conditions one is so routinely accustomed to in dealing with the inhomogeneous systems. What results is a number of simplified and compact forms of the response functions which one only needs to sum up in order to proceed further for studying the desired physical property of the resultant system at hand. Conceptually, this is achieved by stressing that c (the speed of light) and ϵ (the dielectric constant/function) vanish inside the specific region. In order to create a medium bounded by a black-box surface, we assume that Eqs. (2.5)–(2.8) are only valid for either $\rho > R$ or $\rho < R$, with R as the radius of the only cylinder in question by now. Then we multiply the right-hand sides of Eqs. (2.5)–(2.8) by the step function $\theta(\rho - R)$ or $\theta(R - \rho)$, as the case may be. We first calculate the two derivatives needed to evaluate Eqs. (2.9) and (2.10). The results are

$$\begin{aligned} \frac{\partial}{\partial \rho} (\rho E_y) = \frac{1}{\alpha^2} & \left\{ \left[i q_0 \frac{\partial}{\partial \rho} B_z + i q_0 \rho \frac{\partial^2}{\partial \rho^2} B_z - i k \frac{\partial}{\partial \theta} \frac{\partial}{\partial \rho} E_z \right] \right. \\ & \left. - \delta(R - \rho) \left[i q_0 \rho \frac{\partial}{\partial \rho} B_z - i k \frac{\partial}{\partial \theta} E_z \right] \right\} \quad (2.12) \end{aligned}$$

and

$$\begin{aligned} \frac{\partial}{\partial \rho} (\rho B_y) & = \frac{1}{\alpha^2} \left\{ \left[-i q_0 \epsilon \frac{\partial}{\partial \rho} E_z + i q_0 \epsilon \rho \frac{\partial^2}{\partial \rho^2} E_z - i k \frac{\partial}{\partial \theta} \frac{\partial}{\partial \rho} B_z \right] \right. \\ & \left. - \delta(R - \rho) \left[-i q_0 \epsilon \rho \frac{\partial}{\partial \rho} E_z - i k \frac{\partial}{\partial \theta} B_z \right] \right\}. \quad (2.13) \end{aligned}$$

Evidently, the step function (and hence the delta function) dictates the kind of physical situation we will consider in what follows. Then the differential equations (2.9) and (2.10) satisfied by $E_z(\rho, \theta)$ and $B_z(\rho, \theta)$ assume the following forms:

$$\begin{aligned} \left(\frac{-i q_0 \epsilon}{\beta^2} \right) & \left[\left(\frac{\partial^2}{\partial \rho^2} + \frac{1}{\rho} \frac{\partial}{\partial \rho} + \frac{1}{\rho^2} \frac{\partial^2}{\partial \theta^2} + \beta^2 \right) E_z \right. \\ & \left. - \delta(R - \rho) \left(\frac{\partial}{\partial \rho} E_z + \frac{k}{q_0 \epsilon \rho} \frac{\partial}{\partial \theta} B_z \right) \right] = 0 \quad (2.14) \end{aligned}$$

and

$$\begin{aligned} \left(\frac{i q_0}{\beta^2} \right) & \left[\left(\frac{\partial^2}{\partial \rho^2} + \frac{1}{\rho} \frac{\partial}{\partial \rho} + \frac{1}{\rho^2} \frac{\partial^2}{\partial \theta^2} + \beta^2 \right) B_z \right. \\ & \left. - \delta(R - \rho) \left(\frac{\partial}{\partial \rho} B_z - \frac{k}{q_0 \rho} \frac{\partial}{\partial \theta} E_z \right) \right] = 0, \quad (2.15) \end{aligned}$$

where $\beta^2 = -\alpha^2 = q_0^2 \epsilon - k^2$. The formal equations (2.14) and (2.15) will be the standard format for all the calculations of the Green functions of the system of interest in what follows.

Next, let $\vec{r} \equiv (\rho, \theta)$, $\vec{r}' \equiv (\rho', \theta')$, and define the Green function

$$G(\vec{r}, \vec{r}') \equiv G(|\vec{r} - \vec{r}'|) \equiv G(\rho, \theta; \rho', \theta') \quad (2.16)$$

for the homogeneous (bulk) medium [see Eq. (2.11)]:

$$\begin{aligned} \left(\frac{\partial^2}{\partial \rho^2} + \frac{1}{\rho} \frac{\partial}{\partial \rho} + \frac{1}{\rho^2} \frac{\partial^2}{\partial \theta^2} + \beta^2 \right) & G(\vec{r}, \vec{r}') \\ = -4\pi \delta(\vec{r} - \vec{r}') & = -\frac{4\pi}{\rho} \delta(\rho - \rho') \delta(\theta - \theta'). \quad (2.17) \end{aligned}$$

The solution of this equation is given by (see, for example, Ref. 12):

$$G(\vec{r}, \vec{r}') = \sum_{m=-\infty}^{\infty} e^{im(\theta - \theta')} G(m; \rho, \rho'), \quad (2.18)$$

with

$$G(m; \rho, \rho') = i\pi \begin{cases} J_m(\beta\rho) H_m(\beta\rho') & \text{if } \rho \leq \rho' \\ H_m(\beta\rho) J_m(\beta\rho') & \text{if } \rho \geq \rho', \end{cases} \quad (2.19)$$

where $J_m(z)$ [$H_m(z)$] refers to the Bessel function of the first (third) kind of (integer) order m . We write

$$G(m; \rho, \rho') = i\pi \{ [1 - \theta(\rho - \rho')] J_m(\beta\rho) H_m(\beta\rho') + \theta(\rho - \rho') H_m(\beta\rho) J_m(\beta\rho') \}, \quad (2.20)$$

where $\theta(x) = 1(0)$ for $x > 0(x < 0)$ is the Heaviside step function. It is a simple matter to verify that the Green function in Eq. (2.19) represents the exact solution of Eq. (2.18).

We close this section by writing the bulk Green-function tensor for the field components E_z and B_z as a 2×2 matrix:

$$\begin{bmatrix} \left(\frac{-q_0^2 \epsilon}{\beta^2} \right) \left[\frac{\partial^2}{\partial \rho^2} + \frac{1}{\rho} \frac{\partial}{\partial \rho} - \frac{m^2}{\rho^2} + \beta^2 \right] & 0 \\ 0 & \left(\frac{-q_0^2}{\beta^2} \right) \left[\frac{\partial^2}{\partial \rho^2} + \frac{1}{\rho} \frac{\partial}{\partial \rho} - \frac{m^2}{\rho^2} + \beta^2 \right] \end{bmatrix} \times \begin{bmatrix} G_E(m; \rho, \rho') & 0 \\ 0 & G_B(m; \rho, \rho') \end{bmatrix} = -\frac{2}{\rho} \delta(\rho - \rho') \begin{bmatrix} 1 & 0 \\ 0 & 1 \end{bmatrix}, \quad (2.21)$$

where we use $\partial/\partial\theta = im$ and [see Eq. (2.19)]

$$\begin{aligned} -\left(\frac{q_0^2 \epsilon}{\beta^2} \right) G_E(m; \rho, \rho') &= -\left(\frac{q_0^2}{\beta^2} \right) G_B(m; \rho, \rho') \\ &= i\pi \begin{cases} J_m(\beta\rho) H_m(\beta\rho'), & \rho \leq \rho' \\ H_m(\beta\rho) J_m(\beta\rho'), & \rho \geq \rho'. \end{cases} \end{aligned} \quad (2.22)$$

In what follows, we will consider three types of perturbative operations to have the desired results for the resultant structure at hand. In doing so, we will abide by the conceptual scheme of the IRT (see Ref. 4).

III. FORMALISM FOR INVERSE RESPONSE FUNCTIONS

In this section, we will consider three perturbative operations represented geometrically by Fig. 1. Specifically, Figs. 1(A), 1(B), and 1(C) correspond, respectively, to the plasma cylinder of radius R_1 surrounded by a black box surface, a black box cylinder of radius R_2 surrounded by a plasma medium, and a plasma shell sandwiched between the black box cylinder of radius R_1 and a semi-infinite black box surface outside a cylinder of radius R_2 . The plasma media in the perturbations A, B, and C are, in general, characterized by the local dielectric functions $\epsilon_1(\omega)$, $\epsilon_2(\omega)$, and $\epsilon_3(\omega)$, respectively. We will consider the effect of retardation but neglect the absorption throughout. Any subscript $i \equiv 1, 2$, or 3 on the physical quantities should be understood referring to the respective perturbation until and unless stated otherwise.

A. First perturbation

The first perturbation [represented by Fig. 1(A)] is specified by a step function $\theta(R_1 - \rho)$ in front of Eqs. (2.5)–(2.8).

That means that the black-box cleavage operator $\tilde{V}_1(R_1, \rho') \delta(R_1 - \rho')$ is defined such that [see Eqs. (2.14) and (2.15)]

$$\tilde{V}_1(R_1, \rho') = \frac{R_1}{2} \frac{q_0^2}{\beta_1^2} \begin{bmatrix} -\epsilon_1 \frac{\partial}{\partial \rho'} & -\frac{imk}{q_0 \rho'} \\ \frac{imk}{q_0 \rho'} & -\frac{\partial}{\partial \rho'} \end{bmatrix}, \quad (3.1)$$

and the corresponding bulk Green function is written as [see Eqs. (2.22)]

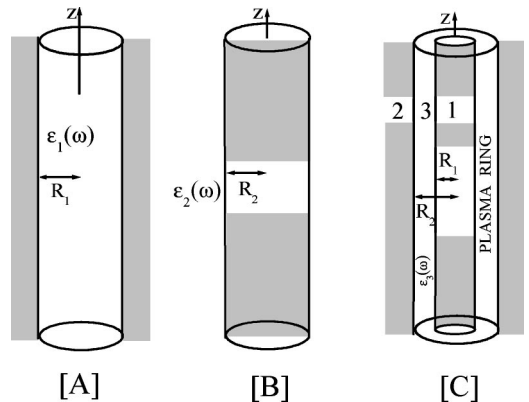


FIG. 1. Schematics of the concept of three perturbations: [A], [B], and [C]. The blank (shaded) region refers to the material medium (black box) in the system. The sum of the first two perturbations defines a plasma (dielectric) cylinder embedded in a dielectric (plasma) and the sum of all three perturbations specifies, say, a plasma (dielectric) shell surrounded by two unidentical dielectrics (plasmas).

$$\tilde{G}_1(\rho, \rho') = i\pi \frac{\beta_1^2}{q_0^2} \begin{bmatrix} -\frac{1}{\epsilon_1} H_m(\beta_1 \rho) J_m(\beta_1 \rho') & 0 \\ 0 & -H_m(\beta_1 \rho) J_m(\beta_1 \rho') \end{bmatrix}. \quad (3.2)$$

It is noteworthy that although the operators \tilde{V}_1 and \tilde{A}_1 as well as the functions \tilde{G}_1 and \tilde{g}_1 are all functions of the variables such as m, k , and ω , we have suppressed them throughout for the sake of brevity and convenience. With this, we define the response operator

$$\tilde{A}_1(R_1, R_1) = \tilde{V}_1(R_1, \rho) \tilde{G}_1(\rho, \rho') |_{\rho=R_1=\rho'} = \begin{bmatrix} \frac{i\pi}{2} \beta_1 R_1 H'_m(\beta_1 R_1) J_m(\beta_1 R_1) & -\frac{\pi}{2} \frac{mk}{q_0} H_m(\beta_1 R_1) J_m(\beta_1 R_1) \\ \frac{\pi}{2} \frac{mk}{q_0 \epsilon_1} H_m(\beta_1 R_1) J_m(\beta_1 R_1) & \frac{i\pi}{2} \beta_1 R_1 H'_m(\beta_1 R_1) J_m(\beta_1 R_1) \end{bmatrix}. \quad (3.3)$$

The prime on the Bessel functions stands for the derivative of the respective quantity with respect to the full argument. Next we define an operator

$$\tilde{\Delta}_1(R_1, R_1) = \tilde{I} + \tilde{A}_1(R_1, R_1) = \begin{bmatrix} \frac{i\pi}{2} \beta_1 R_1 H_m(\beta_1 R_1) J'_m(\beta_1 R_1) & -\frac{\pi}{2} \frac{mk}{q_0} H_m(\beta_1 R_1) J_m(\beta_1 R_1) \\ \frac{\pi}{2} \frac{mk}{q_0 \epsilon_1} H_m(\beta_1 R_1) J_m(\beta_1 R_1) & \frac{i\pi}{2} \beta_1 R_1 H_m(\beta_1 R_1) J'_m(\beta_1 R_1) \end{bmatrix}. \quad (3.4)$$

It should be pointed out that in writing the second equality in Eq. (3.4), we have made use of the identity¹³

$$\frac{1}{J_\nu(z) H_\nu(z)} = \frac{\pi z}{2i} \left[\frac{H'_\nu(z)}{H_\nu(z)} - \frac{J'_\nu(z)}{J_\nu(z)} \right]. \quad (3.5)$$

$$\begin{aligned} \tilde{g}_1^{-1}(R_1, R_1) &= \frac{q_0^2}{2\beta_1^2} \begin{bmatrix} -\beta_1 R_1 \epsilon_1 \frac{J'_m(\beta_1 R_1)}{J_m(\beta_1 R_1)} & -\frac{imk}{q_0} \\ \frac{imk}{q_0} & -\beta_1 R_1 \frac{J'_m(\beta_1 R_1)}{J_m(\beta_1 R_1)} \end{bmatrix} \\ & \quad (3.8) \end{aligned}$$

Next, we calculate the inverse of \tilde{G}_1 to write

$$\tilde{G}_1^{-1}(R_1, R_1) = \frac{q_0^2}{i\pi\beta_1^2} \frac{1}{H_m(\beta_1 R_1) J_m(\beta_1 R_1)} \begin{bmatrix} -\epsilon_1 & 0 \\ 0 & -1 \end{bmatrix}. \quad (3.6)$$

As such, we have all that we need to calculate the inverse response function in the interface space M defined by

$$\tilde{g}_1^{-1}(R_1, R_1) = \tilde{\Delta}_1(R_1, R_1) \tilde{G}_1^{-1}(R_1, R_1). \quad (3.7)$$

represents the response function of a dielectric cylinder surrounded by a black box.

B. Second perturbation

The second perturbation [represented by Fig. 1(B)] is specified by a step function $\theta(\rho - R_2)$ in front of Eqs. (2.5)–(2.8). Then the black-box cleavage operator $\tilde{V}_2(R_2, \rho') \delta(\rho' - R_2)$ is defined such that

$$\tilde{V}_2(R_2, \rho') = -\frac{R_2}{2} \frac{q_0^2}{\beta_2^2} \begin{bmatrix} -\epsilon_2 \frac{\partial}{\partial \rho'} & -\frac{imk}{q_0 \rho'} \\ \frac{imk}{q_0 \rho'} & -\frac{\partial}{\partial \rho'} \end{bmatrix}, \quad (3.9)$$

The result is that

and the corresponding bulk Green function is written as

$$\tilde{G}_2(\rho, \rho') = i\pi \frac{\beta_2^2}{q_0^2} \begin{bmatrix} -\frac{1}{\epsilon_2} J_m(\beta_2 \rho) H_m(\beta_2 \rho') & 0 \\ 0 & -J_m(\beta_2 \rho) H_m(\beta_2 \rho') \end{bmatrix}. \quad (3.10)$$

With this, we define the response operator

$$\tilde{A}_2(R_2, R_2) = \tilde{V}_2(R_2, \rho) \tilde{G}_2(\rho, \rho') |_{\rho=R_2=\rho'} = \begin{bmatrix} -\frac{i\pi}{2} \beta_2 R_2 J'_m(\beta_2 R_2) H_m(\beta_2 R_2) & +\frac{\pi}{2} \frac{mk}{q_0} J_m(\beta_2 R_2) H_m(\beta_2 R_2) \\ -\frac{\pi}{2} \frac{mk}{q_0 \epsilon_2} J_m(\beta_2 R_2) H_m(\beta_2 R_2) & -\frac{i\pi}{2} \beta_2 R_2 J'_m(\beta_2 R_2) H_m(\beta_2 R_2) \end{bmatrix}. \quad (3.11)$$

Next we define an operator

$$\tilde{\Delta}_2(R_2, R_2) = \tilde{I} + \tilde{A}_2(R_2, R_2) = \begin{bmatrix} -\frac{i\pi}{2} \beta_2 R_2 J_m(\beta_2 R_2) H'_m(\beta_2 R_2) & +\frac{\pi}{2} \frac{mk}{q_0} J_m(\beta_2 R_2) H_m(\beta_2 R_2) \\ -\frac{\pi}{2} \frac{mk}{q_0 \epsilon_2} J_m(\beta_2 R_2) H_m(\beta_2 R_2) & -\frac{i\pi}{2} \beta_1 R_2 J_m(\beta_2 R_2) H'_m(\beta_2 R_2) \end{bmatrix}. \quad (3.12)$$

Again, in writing the second equality in Eq. (3.12), we have made use of the identity in Eq. (3.5). Next, we calculate the inverse of \tilde{G}_2 to write

$$\tilde{G}_2^{-1}(R_2, R_2) = \frac{q_0^2}{i\pi \beta_2^2} \frac{1}{J_m(\beta_2 R_2) H_m(\beta_2 R_2)} \begin{bmatrix} -\epsilon_2 & 0 \\ 0 & -1 \end{bmatrix}. \quad (3.13)$$

Now we need to calculate the inverse response function in the interface space M defined by

$$\tilde{g}_2^{-1}(R_2, R_2) = \tilde{\Delta}_2(R_2, R_2) \tilde{G}_2^{-1}(R_2, R_2). \quad (3.14)$$

The result is that

$$\tilde{V}_3(R_i, \rho') = \frac{1}{2} \frac{q_0^2}{\beta_3^2} \begin{bmatrix} \epsilon_3 R_1 \frac{\partial}{\partial \rho'} & \frac{imk}{q_0 \rho'} R_1 & 0 & 0 \\ -\frac{imk}{q_0 \rho'} R_1 & R_1 \frac{\partial}{\partial \rho'} & 0 & 0 \\ 0 & 0 & -\epsilon_3 R_2 \frac{\partial}{\partial \rho'} & -\frac{imk}{q_0 \rho'} R_2 \\ 0 & 0 & \frac{imk}{q_0 \rho'} R_2 & -R_2 \frac{\partial}{\partial \rho'} \end{bmatrix}. \quad (3.16)$$

$$\tilde{g}_2^{-1}(R_2, R_2)$$

$$= \frac{q_0^2}{2\beta_2^2} \begin{bmatrix} \beta_2 R_2 \epsilon_2 \frac{H'_m(\beta_2 R_2)}{H_m(\beta_2 R_2)} & \frac{imk}{q_0} \\ -\frac{imk}{q_0} & \beta_2 R_2 \frac{H'_m(\beta_2 R_2)}{H_m(\beta_2 R_2)} \end{bmatrix} \quad (3.15)$$

represents the response function of black box surrounded by a dielectric medium.

C. Third perturbation

The third perturbation [represented by Fig. 1(C)] is specified by a step function [$\theta(\rho - R_1) - \theta(\rho - R_2)$] in front of Eqs. (2.5)–(2.8). Then the black-box cleavage operator $\tilde{V}_3(R_i, \rho') \delta(\rho' - R_i) P_{nn'}$ [with $P_{nn'} = 1(0)$ for $n, n' \leq 2$ and ≥ 3 (otherwise); $i = 1(2)$ for $n, n' \leq 2$ (≥ 3)] is defined such that

The corresponding bulk Green function is written as

$$\tilde{G}_3(M, M) = i\pi \frac{\beta_3^2}{q_0^2} \begin{bmatrix} -\frac{1}{\epsilon_3} J_m(\beta_3 \rho) H_m(\beta_3 \rho') & 0 & -\frac{1}{\epsilon_3} J_m(\beta_3 \rho) H_m(\beta_3 \rho') & 0 \\ 0 & -J_m(\beta_3 \rho) H_m(\beta_3 \rho') & 0 & -J_m(\beta_3 \rho) H_m(\beta_3 \rho') \\ -\frac{1}{\epsilon_3} H_m(\beta_3 \rho) J_m(\beta_3 \rho') & 0 & -\frac{1}{\epsilon_3} H_m(\beta_3 \rho) J_m(\beta_3 \rho') & 0 \\ 0 & -H_m(\beta_3 \rho) J_m(\beta_3 \rho') & 0 & -H_m(\beta_3 \rho) J_m(\beta_3 \rho') \end{bmatrix}, \quad (3.17)$$

where the interface space M will be referred to as $(\rho=R_1, \rho'=R_1)$, $(\rho=R_1, \rho'=R_2)$, $(\rho=R_2, \rho'=R_1)$ and $(\rho=R_2, \rho'=R_2)$, respectively, in the first, second, third, and fourth quadrants made up of 2×2 submatrices starting clockwise from the top-left. With this, we define the response operator

$$\tilde{A}_3(M, M) = \tilde{V}_3(M) \tilde{G}_3(M, M) = \frac{i\pi}{2} \begin{bmatrix} -\beta_3 R_1 J'_m(\beta_3 R_1) H_m(\beta_3 R_1) - \frac{imk}{q_0} J_m(\beta_3 R_1) H_m(\beta_3 R_1) & -\beta_3 R_1 J'_m(\beta_3 R_1) H_m(\beta_3 R_2) & -\frac{imk}{q_0} J_m(\beta_3 R_1) H_m(\beta_3 R_2) \\ \frac{imk}{q_0 \epsilon_3} J_m(\beta_3 R_1) H_m(\beta_3 R_1) & -\beta_3 R_1 J'_m(\beta_3 R_1) H_m(\beta_3 R_1) & \frac{imk}{q_0 \epsilon_3} J_m(\beta_3 R_1) H_m(\beta_3 R_2) & -\beta_3 R_1 J'_m(\beta_3 R_1) H_m(\beta_3 R_2) \\ \beta_3 R_2 H'_m(\beta_3 R_2) J_m(\beta_3 R_1) & \frac{imk}{q_0} H_m(\beta_3 R_2) J_m(\beta_3 R_1) & \beta_3 R_2 H'_m(\beta_3 R_2) J_m(\beta_3 R_2) & \frac{imk}{q_0} H_m(\beta_3 R_2) J_m(\beta_3 R_2) \\ -\frac{imk}{q_0 \epsilon_3} H_m(\beta_3 R_2) J_m(\beta_3 R_1) & \beta_3 R_2 H'_m(\beta_3 R_2) J_m(\beta_3 R_1) & -\frac{imk}{q_0 \epsilon_3} H_m(\beta_3 R_2) J_m(\beta_3 R_2) & \beta_3 R_2 H'_m(\beta_3 R_2) J_m(\beta_3 R_2) \end{bmatrix}. \quad (3.18)$$

Now we define an operator

$$\tilde{\Delta}_3(M, M) = \tilde{I} + \tilde{A}_3(M, M) = \frac{i\pi}{2} \begin{bmatrix} -\beta_3 R_1 H'_m(\beta_3 R_1) J_m(\beta_3 R_1) - \frac{imk}{q_0} J_m(\beta_3 R_1) H_m(\beta_3 R_1) & -\beta_3 R_1 J'_m(\beta_3 R_1) H_m(\beta_3 R_2) & -\frac{imk}{q_0} J_m(\beta_3 R_1) H_m(\beta_3 R_2) \\ \frac{imk}{q_0 \epsilon_3} J_m(\beta_3 R_1) H_m(\beta_3 R_1) & -\beta_3 R_1 H'_m(\beta_3 R_1) J_m(\beta_3 R_1) & \frac{imk}{q_0 \epsilon_3} J_m(\beta_3 R_1) H_m(\beta_3 R_2) & -\beta_3 R_1 J'_m(\beta_3 R_1) H_m(\beta_3 R_2) \\ \beta_3 R_2 H'_m(\beta_3 R_2) J_m(\beta_3 R_1) & \frac{imk}{q_0} H_m(\beta_3 R_2) J_m(\beta_3 R_1) & \beta_3 R_2 J'_m(\beta_3 R_2) H_m(\beta_3 R_2) & \frac{imk}{q_0} H_m(\beta_3 R_2) J_m(\beta_3 R_2) \\ -\frac{imk}{q_0 \epsilon_3} H_m(\beta_3 R_2) J_m(\beta_3 R_1) & \beta_3 R_2 H'_m(\beta_3 R_2) J_m(\beta_3 R_1) & -\frac{imk}{q_0 \epsilon_3} H_m(\beta_3 R_2) J_m(\beta_3 R_2) & \beta_3 R_2 J'_m(\beta_3 R_2) H_m(\beta_3 R_2) \end{bmatrix}. \quad (3.19)$$

Again, in writing the second equality in Eq. (3.19), we have made use of the identity in Eq. (3.5). Next, we calculate the inverse of the bulk Green function \tilde{G}_3 to write

$$\tilde{G}_3^{-1}(M, M) = \frac{q_0^2}{i\pi\beta_3^2} \frac{1}{D} \begin{bmatrix} -\epsilon_3 \frac{J_m(\beta_3 R_2)}{J_m(\beta_3 R_1)} & 0 & \epsilon_3 & 0 \\ 0 & -\frac{J_m(\beta_3 R_2)}{J_m(\beta_3 R_1)} & 0 & 1 \\ \epsilon_3 & 0 & -\epsilon_3 \frac{H_m(\beta_3 R_1)}{H_m(\beta_3 R_2)} & 0 \\ 0 & 1 & 0 & -\frac{H_m(\beta_3 R_1)}{H_m(\beta_3 R_2)} \end{bmatrix}, \quad (3.20)$$

where the symbol D is defined as

$$D = H_m(\beta_3 R_1)J_m(\beta_3 R_2) - J_m(\beta_3 R_1)H_m(\beta_3 R_2). \quad (3.21)$$

Finally, we calculate the inverse response function of a cylindrical shell bounded by two black boxes

$$\tilde{g}_3^{-1}(M, M) = \tilde{\Delta}_3(M, M)\tilde{G}_3^{-1}(M, M), \quad (3.22)$$

to write

$$\tilde{g}_3^{-1}(M, M) = \frac{q_0^2}{2\beta_3^2} \begin{bmatrix} \beta_3 R_1 \epsilon_3 \frac{Z_1}{D} & \frac{imk}{q_0} & -\frac{2i\epsilon_3}{\pi D} & 0 \\ -\frac{imk}{q_0} & \beta_3 R_1 \frac{Z_1}{D} & 0 & -\frac{2i}{\pi D} \\ -\frac{2i\epsilon_3}{\pi D} & 0 & \beta_3 R_2 \epsilon_3 \frac{Z_2}{D} & -\frac{imk}{q_0} \\ 0 & -\frac{2i}{\pi D} & \frac{imk}{q_0} & \beta_3 R_2 \frac{Z_2}{D} \end{bmatrix}, \quad (3.23)$$

where

$$Z_1 = H'_m(\beta_3 R_1)J_m(\beta_3 R_2) - J'_m(\beta_3 R_1)H_m(\beta_3 R_2),$$

$$Z_2 = H'_m(\beta_3 R_2)J_m(\beta_3 R_1) - J'_m(\beta_3 R_2)H_m(\beta_3 R_1). \quad (3.24)$$

Having calculated the inverse response functions for the three perturbations, it becomes an easy task to deduce the dispersion relations for the plasmon propagation in the real physical systems. These are (i) a plasma (dielectric) cylinder embedded in a dielectric (plasma) and (ii) a plasma (dielectric) shell surrounded by two unidentical dielectrics (plasmas), for example. This is what we intend to do in what follows.

D. Plasma (dielectric) cylinder embedded in dielectric (plasma)

Merger of perturbations A and B results into a geometry of a plasma (dielectric) cylinder embedded in a dielectric (plasma). As such, one can write $\tilde{g}^{-1} = \tilde{g}_1^{-1} + \tilde{g}_2^{-1}$, where \tilde{g}^{-1} is the inverse response function of a single cylinder in a semi-infinite medium. That means that formally the determinant of the sum of inverse response functions in Eqs. (3.8) and (3.15), with $R_1 = R = R_2$, equated to zero, i.e.,

$$|\tilde{g}^{-1}(M, M)| = |\tilde{g}_1^{-1}(M, M) + \tilde{g}_2^{-1}(M, M)| = 0, \quad (3.25)$$

should yield the dispersion relation for plasmons with a mixed (TM and TE) character in a single cylindrical geometry. The result is

$$\left| \begin{array}{c} -\left[\frac{q_0 \epsilon_1 J'_m(\beta_1 R)}{\beta_1 J_m(\beta_1 R)} - \frac{q_0 \epsilon_2 H'_m(\beta_2 R)}{\beta_2 H_m(\beta_2 R)} \right] \\ \frac{imk}{R} \left(\frac{1}{\beta_1^2} - \frac{1}{\beta_2^2} \right) \end{array} \right| = 0 \quad (3.26)$$

or

$$\left[\frac{\epsilon_1 J'_m(\beta_1 R)}{\beta_1 J_m(\beta_1 R)} - \frac{\epsilon_2 H'_m(\beta_2 R)}{\beta_2 H_m(\beta_2 R)} \right] \left[\frac{1 J'_m(\beta_1 R)}{\beta_1 J_m(\beta_1 R)} - \frac{1 H'_m(\beta_2 R)}{\beta_2 H_m(\beta_2 R)} \right] = \left(\frac{m}{R} \right)^2 \frac{k^2}{q_0^2} \left(\frac{1}{\beta_1^2} - \frac{1}{\beta_2^2} \right)^2. \quad (3.27)$$

This expression is exactly identical to Eq. (107) in Ref. 14, which was obtained through the use of messy boundary conditions decades ago by Stratton. Only in the special limit of $m=0$ can the TM (represented by the first square bracket equated to zero) and TE (specified by the second square bracket equated to zero) modes become separable. We concentrate on the TM modes for studying, for example, plasmons in a slender wire made up of the cylinder in the limit $R \rightarrow 0$.

Quantum wire in the electric quantum limit

For $m=0$, the TM modes are characterized by the following dispersion law:

$$\frac{\epsilon_1 J_1(\beta_1 R)}{\beta_1 J_0(\beta_1 R)} - \frac{\epsilon_2 H_1(\beta_2 R)}{\beta_2 H_0(\beta_2 R)} = 0, \quad (3.28)$$

since $\zeta'_0 = -\zeta_1$, with $\zeta_m \equiv J_m, H_m$. It is not difficult to prove that Eq. (3.28) is exactly identical to Eq. (18) in Ref. 15, which was also derived through the use of boundary conditions, and represents the plasmon dispersion for the classical dielectric waveguide. It is a simple matter to understand that in order to be able to deduce some expected results for the planar interface we need to employ the large-argument limit (i.e., $R \rightarrow \infty$). Imposing asymptotic expansions of the Bessel functions for large arguments (i.e., when $H_1/H_0 = i$ and $J_1/J_0 = -i$), we obtain $\epsilon_1 \beta_2 + \epsilon_2 \beta_1 = 0$, which is a well-known general dispersion law for the TM modes propagating on an interface between two unidentical media characterized by dielectric functions ϵ_1 and ϵ_2 (see, for example, Ref. 1); here β_1 and β_2 serve as the decay constants for the respective media and have to be purely imaginary for the plasmon-polaritons.

Intuitively, a macroscopic plasma cylinder with a vanishingly small radius should mimic a fashionable quantum wire and hence one would expect such a semiclassical methodology as treated here to reproduce the corresponding *intrasubband* plasmon dispersion. Using the lowest-order expansions of the involved Bessel functions for the small arguments one can cast Eq. (3.28) in the form

$$\epsilon_1 + \frac{2\epsilon_2 K_1(\alpha_2 R)}{\alpha_2 R K_0(\alpha_2 R)} = 0, \quad (3.29)$$

where $\alpha_2 = (k^2 - q_0^2 \epsilon_2)^{1/2}$ refers to the decay constant in the outer background medium. For outer medium as a dielectric, small radius ($R \rightarrow 0$), and long wavelength limit, the modified Bessel functions K_0 and K_1 are both positive. Therefore in order to obtain a bonafide solution of this equation, the dielectric function ϵ_1 must be negative. This means that in the local approximation only the frequencies below the screened plasma frequency should make sense. In the limit of a small radius, Eq. (3.28) can also be written as

$$\omega = \omega_0 \cdot \beta_2 R \cdot |\ln(\beta_2 R)|^{1/2}, \quad (3.30)$$

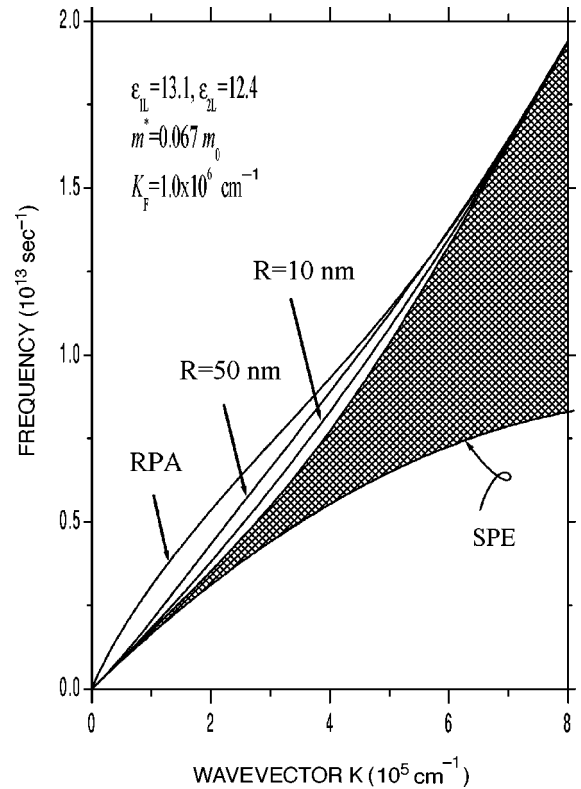


FIG. 2. Computed plasmon dispersion in a quantum wire. The curve marked RPA and the hatched region labeled SPE (single-particle excitations) are based on the RPA with $\epsilon_{RPA} = 0$. The two curves marked with the specified values of the radii ($R=10$ and 50 nm) are calculated using the present formalism. The parameters used are given inside the figure.

where $\omega_0 = (2\pi n_B e^2 / m^* \epsilon_{2L})^{1/2}$, ϵ_{2L} the background dielectric constant in the outer semiinfinite medium, and n_B the effective 3D carrier density. In its present form, Eq. (3.30) is an exact analog of Eq. (2.13) in Ref. 16, but includes the retardation effect. We have solved Eq. (3.29) for the longitudinal plasmon modes with ϵ_1 replaced by $\epsilon_{RPA}(k, \omega)$. Figure 2 shows the comparative study where we plot the dispersion relations based purely on the zeros of the nonlocal, dynamic dielectric function $\epsilon_{RPA}(k, \omega)$ (see, for example, Ref. 1) and the preceding scheme. The relevant parameters are listed in the figure. As one can notice the longer the wavelength, the larger the deviation from the random phase approximation (RPA) results. At large propagation vector k , the ratio of the two modified Bessel functions approaches unity and the second term, in Eq. (3.29), becomes gradually ineffective and hence the results of the two schemes begin to converge. Similar effects are manifested if we enhance the radius of the cylinder, as an alternative. For instance, the plasmon mode corresponding to $R=50$ nm starts merging with the RPA plasmon at lower k than the one for $R=10$ nm. We have ignored the higher order solutions because they correspond to the unusually large carrier concentration and are irrelevant for the electric quantum limit (i.e., where only the lowest subband is occupied) considered here. The hatched region, though does not make much sense in the present context, refers to the intrasubband single-particle excitation spectrum coming from the RPA scheme. Note that each plasma medium in the system is characterized throughout by a local dielectric function $\epsilon(\omega) = \epsilon_L (1 - \omega_p^2 / \omega^2)$, where ϵ_L is

the background dielectric constant and ω_p the screened plasma frequency, until and unless stated otherwise.

E. Plasma (dielectric) shell bounded by two unidentical dielectrics (plasmas)

In this section we are motivated to study a physical system made up of two coaxial cylinders where we can have the plasma shell bounded by two unidentical dielectrics or a dielectric shell bounded by two unidentical plasmas, in general. We will study diverse situations of practical interest. Methodologically, such a geometry becomes realizable by summing up the inverse response functions calculated in Eqs. (3.8), (3.15), and (3.23) in the interface space M . One can write $\tilde{g}^{-1} = \tilde{g}_1^{-1} + \tilde{g}_2^{-1} + \tilde{g}_3^{-1}$, where \tilde{g}^{-1} is the response function of the finite cylindrical shell surrounded by two, in general, unidentical media. The dispersion relation for plasmons in such a resultant structure is derived by equating the determinant of the total inverse response function to zero, i.e.,

$$|\tilde{g}^{-1}(M, M)| = |\tilde{g}_1^{-1}(M, M) + \tilde{g}_2^{-1}(M, M) + \tilde{g}_3^{-1}(M, M)| = 0. \quad (3.31)$$

After some straightforward mathematical steps, we simplify Eq. (3.31) to write explicitly in the compact form as follows:

$$\begin{vmatrix} -R_1 \left(\frac{\epsilon_1}{\beta_1} A_1 - \frac{\epsilon_3}{\beta_3} C_1 \right) & -\frac{imk}{q_0} \left(\frac{1}{\beta_1^2} - \frac{1}{\beta_3^2} \right) & -\frac{2i\epsilon_3}{\pi\beta_3^2 D} & 0 \\ \frac{imk}{q_0} \left(\frac{1}{\beta_1^2} - \frac{1}{\beta_3^2} \right) & -R_1 \left(\frac{1}{\beta_1} A_1 - \frac{1}{\beta_3} C_1 \right) & 0 & -\frac{2i}{\pi\beta_3^2 D} \\ -\frac{2i\epsilon_3}{\pi\beta_3^2 D} & 0 & R_2 \left(\frac{\epsilon_2}{\beta_2} A_2 + \frac{\epsilon_3}{\beta_3} C_2 \right) & \frac{imk}{q_0} \left(\frac{1}{\beta_2^2} - \frac{1}{\beta_3^2} \right) \\ 0 & -\frac{2i}{\pi\beta_3^2 D} & -\frac{imk}{q_0} \left(\frac{1}{\beta_2^2} - \frac{1}{\beta_3^2} \right) & R_2 \left(\frac{1}{\beta_2} A_2 + \frac{1}{\beta_3} C_2 \right) \end{vmatrix} = 0, \quad (3.32)$$

where the additional substitutions are defined as

$$A_1 = J'_m(\beta_1 R_1) / J_m(\beta_1 R_1),$$

$$A_2 = H'_m(\beta_2 R_2) / H_m(\beta_2 R_2),$$

$$C_1 = Z_1 / D,$$

$$C_2 = Z_2 / D. \quad (3.33)$$

We are now interested to check how Eq. (3.32) can reproduce some well established results. For this purpose, we consider the limit $R_1 \sim R_2 \sim R \rightarrow \infty$ but take $R_2 - R_1 = d$ as

a finite quantity and fix $m=0$. Naturally then, we need to make use of the asymptotic limits of the Bessel functions $J_\nu(z)$ and $H_\nu(z)$. As such, we first simplify the substitutions involved to obtain $A_1=-i$, $A_2=i$, $D=-(2i/\pi$

$\times \alpha_3 R) \sinh(\alpha_2 d)$, $Z_1=Z_2=(2/\pi \alpha_3 R) \cosh(\alpha_3 d)$, and $C_1=C_2=i \coth(\alpha_3 d)$; here $\beta_3=i \alpha_3$ just as before. As a consequence, we simplify the general dispersion relation in Eq. (3.32) to write

$$\begin{vmatrix} R\left(\frac{\epsilon_1}{\alpha_1} + \frac{\epsilon_3}{\alpha_3} C\right) & \frac{imk}{q_0} \left(\frac{1}{\alpha_1^2} - \frac{1}{\alpha_3^2}\right) & -R \frac{\epsilon_3}{\alpha_3} S & 0 \\ -\frac{imk}{q_0} \left(\frac{1}{\alpha_1^2} - \frac{1}{\alpha_3^2}\right) & R\left(\frac{1}{\alpha_1} + \frac{1}{\alpha_3} C\right) & 0 & -R \frac{1}{\alpha_3} S \\ -R \frac{\epsilon_3}{\alpha_3} S & 0 & R\left(\frac{\epsilon_2}{\alpha_2} + \frac{\epsilon_3}{\alpha_3} C\right) & -\frac{imk}{q_0} \left(\frac{1}{\alpha_2^2} - \frac{1}{\alpha_3^2}\right) \\ 0 & -R \frac{1}{\alpha_3} S & \frac{imk}{q_0} \left(\frac{1}{\alpha_2^2} - \frac{1}{\alpha_3^2}\right) & R\left(\frac{1}{\alpha_2} + \frac{1}{\alpha_3} C\right) \end{vmatrix} = 0, \quad (3.34)$$

where $C=\coth \theta$ and $S^{-1}=\sinh \theta$; with $\theta=\alpha_3 d$. Now let us carefully impose the limit $R \rightarrow \infty$. Then it is a simple matter to prove that Eq. (3.34) reduces to the form

$$\left[\frac{1}{\alpha_1 \alpha_2} + \left(\frac{1}{\alpha_1} + \frac{1}{\alpha_2} \right) \frac{1}{\alpha_3} \coth \theta + \left(\frac{1}{\alpha_3} \right)^2 \right] \left[\frac{\epsilon_1 \epsilon_2}{\alpha_1 \alpha_2} + \left(\frac{\epsilon_1}{\alpha_1} + \frac{\epsilon_2}{\alpha_2} \right) \frac{\epsilon_3}{\alpha_3} \coth \theta + \left(\frac{\epsilon_3}{\alpha_3} \right)^2 \right] = 0. \quad (3.35)$$

Either the first or the second factor is zero. It is not quite difficult to prove that the first (second) factor equated to zero yields the TE (TM) modes propagating in the *planar* film geometry. We focus on the second factor to study the 2D plasmons in a quantum well in the limit $d \rightarrow 0$.

Quantum well in the electric quantum limit

The trigonometrical factor $\coth \theta$ in the limit of $\theta \rightarrow 0$ can be expanded in the following approximate form

$$\coth \theta \approx \frac{1}{\theta} + \frac{\theta}{3} - \frac{\theta^3}{45} + \frac{2\theta^5}{945} - \dots, \quad (3.36)$$

where $\theta=\alpha_3 d$. We consider the situation where ϵ_1 and ϵ_2 refer to the dielectric media and ϵ_3 to the plasma. A simple mathematical analysis (in the limit $d \rightarrow 0$ and hence $\epsilon_3 \rightarrow \infty$) also leads us to deduce that $\alpha_3^2 d^2 \rightarrow 0$ and $\epsilon_3 d \approx 4\pi\chi$, with $\chi = -n_s e^2 / m^* \omega^2$ referring to the zero-temperature polarizability function in the long wavelength limit, remains a finite quantity. As such, retaining only the first term in the approximation and equating the second factor in Eq. (3.35) to zero yields

$$4\pi\chi + \frac{\epsilon_1}{\alpha_1} + \frac{\epsilon_2}{\alpha_2} = 0. \quad (3.37)$$

This is now a well-known result that represents the plasma modes of a single 2DEG layer sandwiched between two dielectrics (see, for example, Ref. 1). Furthermore, considering the bounding media to be identical (i.e., $\epsilon_1=\epsilon_2=\epsilon$ and hence $\alpha_1=\alpha_2=\alpha$) and imposing the non-retardation limit (i.e., $q_0=0$ and hence $\alpha=k$) leaves us with

$$\omega^2 = (2\pi n_s e^2 / m^* \epsilon) k, \quad (3.38)$$

where n_s stands for the areal carrier density. This is a standard result for the intrasubband plasmon dispersion in a quantum well, with the plasma frequency $\omega_p \propto \sqrt{k}$.

F. Local and total density of states

The density of states (DOS) is of fundamental importance to the understanding of many physical phenomena in condensed matter physics. The interpretation of quite a number of experimental excitation spectra in a wide variety of systems subjected to different physical conditions requires a detailed knowledge of the DOS. Classic textbooks and monographs reveal that the standard algorithm of determining the density of states is founded on the Green-function approach. Our purpose here is to calculate the local and total DOSs in order to substantiate the computed plasmon modes in the cylindrical geometries at hand. Unless some numeric hurdle comes in way, this is logical to expect that the peaks in the DOS should coincide with the zeros of the inverse response function, which determine the plasmon modes for a given propagation vector, of a system.

1. Local density of states

The formal expression for the local density of states (LDOS) in the framework of interface response theory⁴ is generally quite fussy and as the name suggests requires some subtle details of the local physical conditions. These are, for

example, the basic definitions of the bulk Green functions, the spatial positions around the interface, the nature of the associated electromagnetic fields involved, etc. In the present context, the simplest definition of the LDOS at the expense of a few negligible concerns but that which still contains the important physics involved is given by

$$\mathcal{N}_L(\omega) = -2 \frac{\omega}{\pi} \text{Im}\{\text{Tr}[\tilde{g}(M, M)]\}, \quad (3.39)$$

where \tilde{g} refers to the response function whose inverse was determined in the preceding subsections for diverse situations. The important thing is to understand which system this response function \tilde{g} refers to in different physical situations. We consider two such cases of our interest: a single-interface system (see Sec. III D) and a double-interface system (see Sec. III E). For a single-interface system, \tilde{g} is simply the inverse of the sum of \tilde{g}_1^{-1} and \tilde{g}_2^{-1} (see Sec. III D). In the case of a two-interface system, we need to study the LDOS at the two interfaces R_1 and R_2 independently. For the interface R_1 (R_2) the \tilde{g} in Eq. (3.39) is the 2×2 submatrix in the first (fourth) quadrant of the inverse of the sum of three inverse response functions (see Sec. III E).

2. Total density of states

For the z components of the electromagnetic fields considered here, the analytical expression for the variation of the total density of states (TDOS) within the interface response theory⁴ is given by

$$\mathcal{N}_T(\omega) = -\frac{1}{\pi} \frac{d}{d\omega} \left(\text{Arg det} \begin{bmatrix} \tilde{g}_i(M, M) \\ \tilde{g}_f(M, M) \end{bmatrix} \right). \quad (3.40)$$

By the variation of TDOS we mean the difference between the TDOS of the final (physical) system and an initial system. Here \tilde{g}_i (\tilde{g}_f) stands for the response function of the initial (final) system in question. For the single-interface system, \tilde{g}_i is a product of \tilde{g}_1 and \tilde{g}_2 ; and \tilde{g}_f is the inverse of the sum of \tilde{g}_1^{-1} and \tilde{g}_2^{-1} . In the case of a two-interface system, $\tilde{g}_i = \tilde{g}_{1f} \cdot \tilde{g}_{2f}$, where \tilde{g}_{1f} is the inverse of the sum of a 4×4 matrix comprised of the \tilde{g}_1^{-1} and \tilde{g}_2^{-2} , and \tilde{g}_{2f} is the inverse of \tilde{g}_3^{-1} that corresponds to perturbation 3 for the shell alone; and \tilde{g}_f is the inverse of the sum of \tilde{g}_1^{-1} , \tilde{g}_2^{-1} , and \tilde{g}_3^{-1} . It should be pointed out that both local and total DOSs are computed for every value of integer m .

It is also worth mentioning that in the course of studying the total DOS we have the finite (or bounded) parts of the system automatically incorporated. Therefore, we are bound to find some discrete modes in the TDOS, which usually appear as the negative peaks in the DOS– ω space and do not bear any physical significance if one is only interested in studying the confined or extended plasmon-polaritons. Moreover, if we are interested to understand all the existing peaks in the TDOS, we need to explore, for example, each of the three perturbations involved individually. We have found that while the negative peaks in the individual perturbations sur-

vive in the TDOS, all the positive peaks are seen to disappear. This remains unfaillingly true for all the cases we have investigated both for single- and double-interface systems. All the peaks in the LDOS are always positive. More specific comments will be made later (see Sec. IV).

IV. ILLUSTRATIVE EXAMPLES

As we have seen in the preceding section, our final results for the dispersion characteristics are Eqs. (3.26) and (3.32), respectively, for the single cylinder embedded in some different material background and the coaxial cylindrical geometries. Note that both of these equations are, in general, the complex transcendental functions. Therefore, in principle, we need to search for zeros of such complex functions. Despite much advancement in the software science, searching for reliable zeros of such complex functions is not an easy task. So, we had to strike a compromise among a few choices. We decided to ask the machine to produce those zeros where the real part of the function changes sign, irrespective of whether or not the imaginary part is zero. We believe this has resulted in a reliable scheme for studying the dispersion characteristics of plasmons in the present systems. This is because all the plasmon modes (confined or extended) are found to have an excellent correspondence with

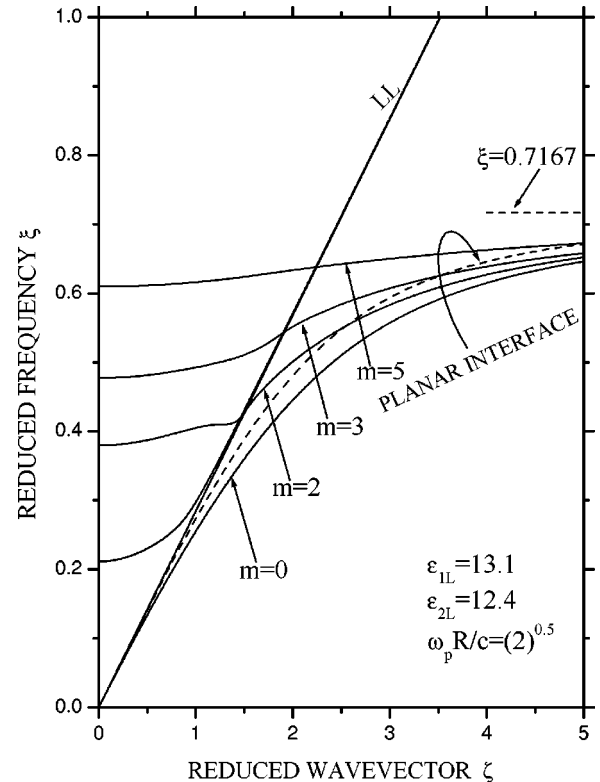


FIG. 3. Plasmon dispersion for a GaAs plasma cylinder ($\epsilon_{1L} = 13.1$) embedded in a $\text{Ga}_{1-x}\text{Al}_x\text{As}$ dielectric ($\epsilon_{2L} = 12.4$). The dimensionless plasma frequency used in the computation is specified by $\omega_p R/c = \sqrt{2}$. The dashed curve refers to the planar interface plasmon polaritons and the dashed horizontal line labeled as $\xi = 0.7167$ indicates the corresponding asymptotic frequency. The solid straight line is the light line in the dielectric background.

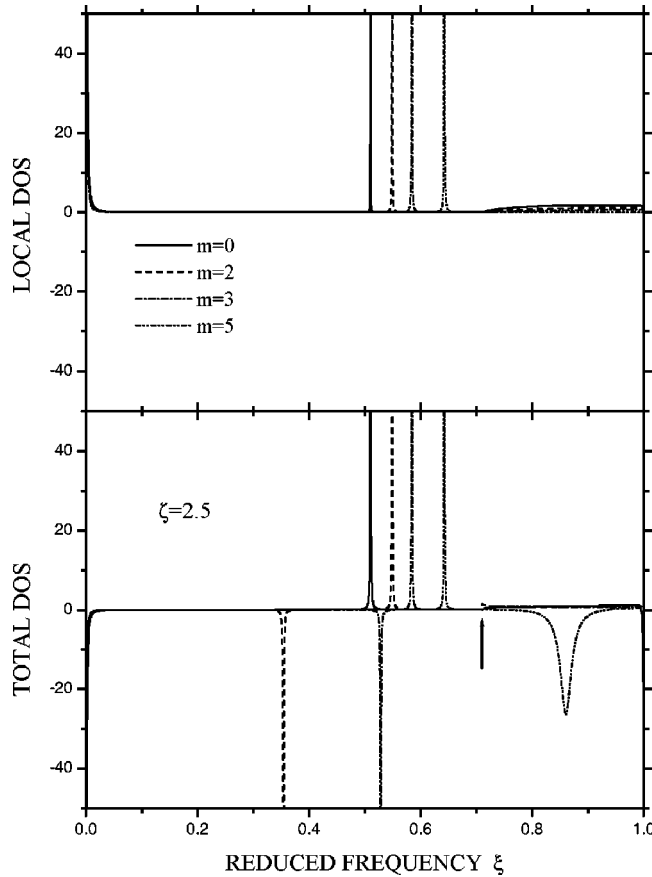


FIG. 4. Local (total) density of states in the upper (lower) panel for various values of m and $\zeta=2.5$. The rest of the parameters used are the same as in Fig. 3. The arrow in the lower panel refers to a small invisible peak at $\xi=0.70995$ where $\beta_2=0$.

the peaks in the local and total density of states. We consider mostly a GaAs plasma, a $\text{Ga}_{1-x}\text{Al}_x\text{As}$ dielectric, and a SiO_2 dielectric with background dielectric constants $\epsilon_L=13.1$, 12.4, and 4.5, respectively. We will later assign an additional numeral to the suffix of the background dielectric constants corresponding to the region in the geometry concerned. Other parameters such as the ratio of the radii of the cylinders R_2/R_1 , the normalized plasma frequency $\omega_p R/c$, and the azimuthal index of the Bessel functions m will be given at the appropriate places during the discussion. We will present our results in terms of the dimensionless propagation vector $\zeta=ck/\omega_p$ and frequency $\xi=\omega/\omega_p$, where ω_p stands for the screened plasma frequency. Both local and total DOSs will be shown in arbitrary units throughout.

A. Plasma (dielectric) cylinder embedded in dielectric (plasma)

Figure 3 shows the plasmon dispersion for a GaAs plasma cylinder in a $\text{Ga}_{1-x}\text{Al}_x\text{As}$ dielectric for $m=0, 2, 3$, and 5 and $\omega_p R/c=\sqrt{2}$. The dotted curve refers to the plasmon-polariton mode for the planar interface, and the dashed horizontal line marked as $\xi=0.7167$ indicates the corresponding asymptotic frequency in the nonretardation limit [i.e., $\xi=(1+\epsilon_{2L}/\epsilon_{1L})^{-1/2}$]. The straight line marked as LL stands for the light line in the dielectric background. It is observed

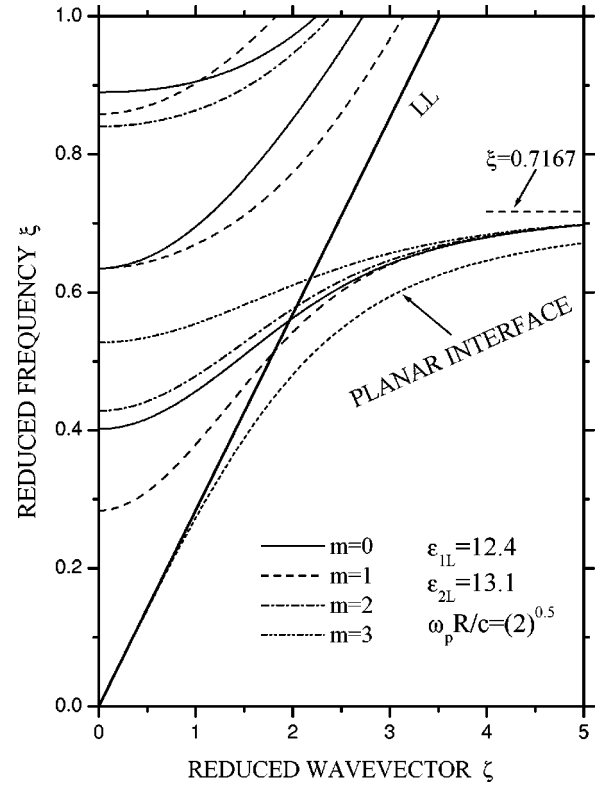


FIG. 5. The same as in Fig. 3 but for the plasmon dispersion for a $\text{Ga}_{1-x}\text{Al}_x\text{As}$ dielectric ($\epsilon_{1L}=12.4$) in GaAs plasma ($\epsilon_{2L}=13.1$). There are four groups of curves for four different values of m .

that there are two modes for every m : one starts in the radiative region (towards the left of the light-line where β_2 is purely real) with a finite frequency and the other at the origin along and towards the right of the light line in the nonradiative region (towards the right of the light line where β_2 is purely imaginary). The former ends up merging with the light line while the latter becomes asymptotic to $\xi=0.7167$. Even at considerably large ζ , all modes retain their character: the larger m , the higher the frequency.

Figure 4 illustrates the local (total) density of states in the upper (lower) panel for $\zeta=2.5$ in the nonradiative region in the $\xi-\zeta$ space for $m=0, 2, 3$, and 5. The rest of the parameters are the same as in Fig. 3. The sharp peaks at $\xi=0.5098, 0.5486, 0.5837$, and 0.6422 are seen to be common to both local and total DOSs. The negative peaks are coming from the second perturbation (see Sec. III) which produces one positive and another negative peak for every m . The positive peak disappears and the negative one survives in the total DOS. The arrow at $\xi=0.70995$ indicates an indiscernibly small negative peak for $m=0$ where β_2 vanishes. We observe a pile up of rather small DOS, both local and total, at $\xi \geq 0.7167$. Every positive peak in the local/total DOS shows an excellent correspondence with the respective confined plasmon mode (in the nonradiative region) in Fig. 3.

Figure 5 depicts the plasmon dispersion for a $\text{Ga}_{1-x}\text{Al}_x\text{As}$ cylinder embedded in a GaAs plasma for $\omega_p R/c=\sqrt{2}$. The solid, dashed, dash-dotted, and dash-dot-dotted curves stand

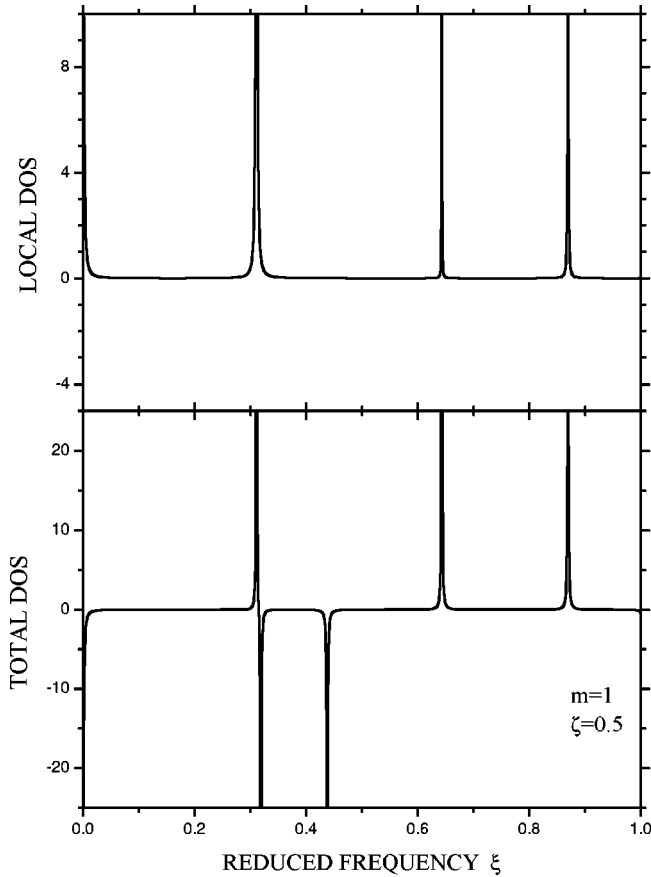


FIG. 6. Local (total) density of states in the upper (lower) panel for $m=1$ and $\zeta=0.5$. The rest of the parameters used are the same as in Fig. 5. The negative peaks in the lower panel emerge from the first perturbation alone and bear no physical significance.

for the plasmon modes, respectively, for $m=0, 1, 2,$ and 3 . The dotted curve represents the plasmon polariton mode for the corresponding planar interface, and the dashed line marked as $\xi=0.7167$ refers to its asymptotic frequency in the nonretardation limit. Unlike Fig. 3, we observe a larger number of radiative modes (in the region towards the left of the light line marked as LL) for every m , even though the number of confined plasmon modes at large ζ is still the same (i.e., one for every m). It is interesting to note that in the present case there is almost a smooth transition of the plasmon propagation in the vicinity of the light line. This contrasts the corresponding behavior in Fig. 3. Also distinguishable is the fact that all the confined modes seem to merge together and lose their identity at smaller values of ζ as compared to the same in Fig. 3. Furthermore, the plasmon mode for the corresponding planar interface is seen to remain the lowest mode in the whole $\xi-\zeta$ space in Fig. 5, unlike the one in Fig. 3.

Figure 6 shows the local (total) density of states in the upper (lower) panel for $m=1$ and $\zeta=0.5$. The other parameters are the same as in Fig. 5. All three positive peaks appearing at $\xi=0.3111, 0.6434,$ and 0.8695 in the local DOS are seen to be consistent with the corresponding positive peaks in the total DOS. These positive peaks showing up in the local and total DOSs are in very good agreement with the

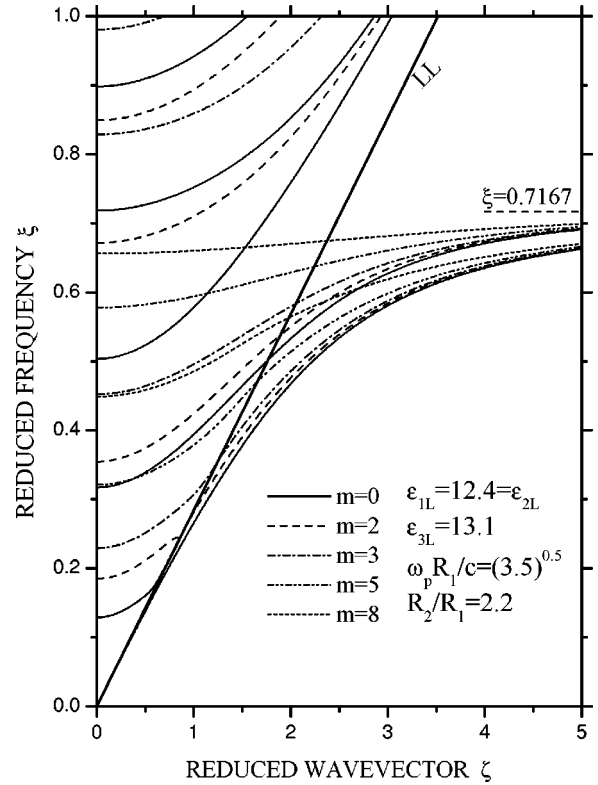


FIG. 7. Plasmon dispersion in a GaAs plasma ($\epsilon_{3L}=13.1$) shell sandwiched between identical $\text{Ga}_{1-x}\text{Al}_x\text{As}$ dielectrics ($\epsilon_{1L}=12.4=\epsilon_{2L}$). There are five groups of curves for five different values of m . The solid straight line labeled as LL refers to the light line in the $\text{Ga}_{1-x}\text{Al}_x\text{As}$ dielectric. The parameters used in the computation are as listed in the picture.

frequencies of the three radiative plasmon modes at $\zeta=0.5$ in Fig. 5. The existence of the two negative peaks at $\xi=0.3190$ and 0.4381 in the total DOS is attributed to the first perturbation alone. It is found that both of the negative peaks are the exact solutions of $|\tilde{g}_1^{-1}|=0$. Moreover, the positive peaks occurring at $\xi=0.14199$ and 0.78243 (where J_1 vanishes) in the first perturbation are seen to disappear from the total DOS.

B. Plasma (dielectric) shell bounded by two dielectrics (plasmas)

Figure 7 illustrates the dispersion relations of the plasmon-polariton modes for the coaxial cylindrical geometry made up of GaAs plasma shell bounded by a $\text{Ga}_{1-x}\text{Al}_x\text{As}$ dielectric both in the inner cylinder and outer semi-infinite media. As for other relevant parameters, we consider $\omega_p R_1/c=\sqrt{3.5}$ and $R_2/R_1=2.2$. The solid, dashed, dash-dotted, dash-dot-dotted, and dotted curves stand for the values of $m=0, 2, 3, 5,$ and 8 . Since the inner and outer media are identical, we still have a single asymptotic frequency in the nonretardation limit $\xi=0.7167$ assigned to the dashed horizontal line. The straight solid line marked as LL is the light line in the dielectric media enclosing the plasma shell. Note that while the number of the confined plasmon modes at large value of ζ (in the nonradiative region) is still

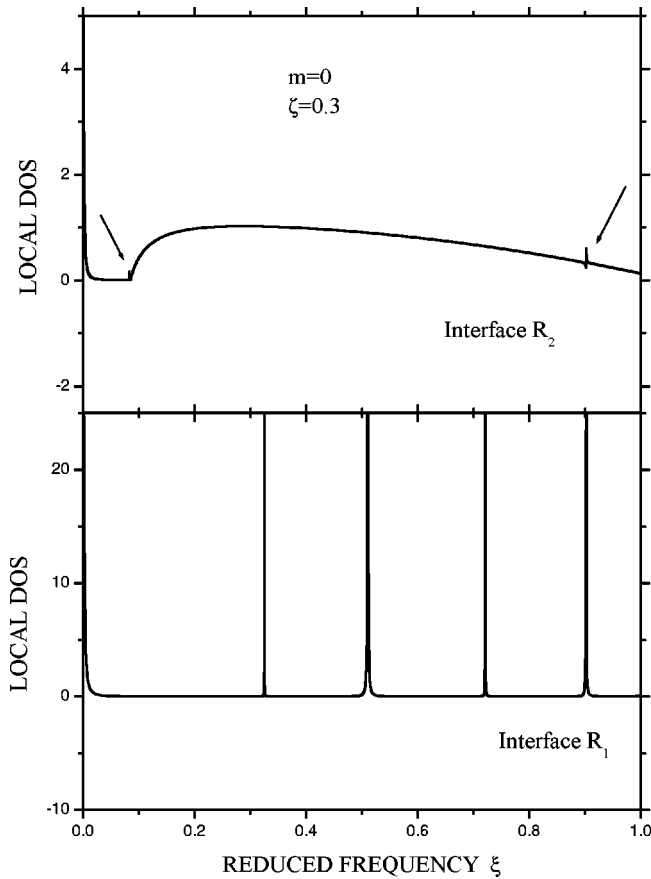


FIG. 8. Local density of states at the interface R_1 (R_2) in the lower (upper) panel for $m=0$ and $\zeta=0.3$. We call attention to the smaller DOS resonances, indicated by arrows, corresponding to the interface R_2 . The rest of the parameters used are the same as in Fig. 7.

two in conformation with the two interfaces in question, there can be any number of extended modes in the radiative region for a given m depending upon the ratio R_2/R_1 .

Figure 8 shows the local density of states at the interface R_1 (R_2) in the lower (upper) panel for $m=0$ and $\zeta=0.3$. The rest of the parameters are the same as in Fig. 7. We note that there are four well defined sharp DOS peaks at $\xi = 0.3252, 0.5107, 0.7213,$ and 0.9023 at the interface R_1 , whereas the interface R_2 captures only two low DOS peaks at $\xi = 0.0835$ and 0.9023 . That means that the two interfaces in the coaxial cylindrical geometry have different preferences. This is the case even though one may argue quite contrarily in view of the fact that the plasma shell is symmetrically bounded by the identical dielectrics. However, it seems that the two interfaces are more sensitive to the geometry and less to the materials in the bounding media. That is to say that the situation is altogether different from a planar geometry with a thin film symmetrically bounded by identical dielectrics. It is noteworthy that only the highest peak in the local DOS is shared by both interfaces, albeit with a difference of magnitude. Moreover, except for the lowest one at the interface R_2 which corresponds to the confined plasmon mode, all the higher resonances explain the radiative modes at this value of ζ .

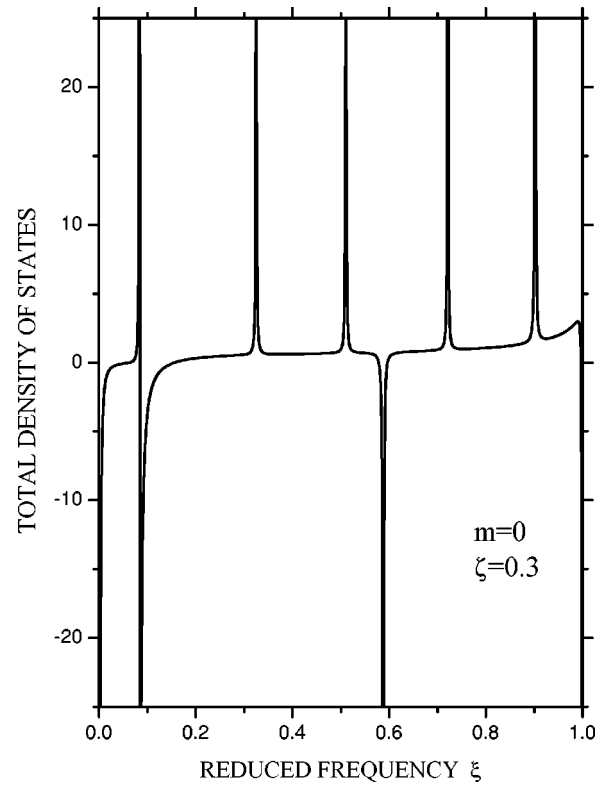


FIG. 9. Total density of states for $m=0$ and $\zeta=0.3$. The higher (lower) negative peak emerges from the first (second) perturbation and has no physical significance. The rest of the parameters used are the same as in Fig. 8.

Figure 9 presents the total density of states for the same system as studied in Figs. 7 and 8 for $m=0$ and $\zeta=0.3$. One can notice at once that there are five positive resonance peaks lying at the same frequencies as those in the local DOS (summing up all the peaks at both interfaces; see above). In addition, there are two negative peaks at $\xi = 0.08519$ and 0.5878 . We explore that the lower (upper) negative peak comes from the second (first) perturbation alone where the Bessel function J_1 vanishes. That is to say that the position of the lower (upper) negative peak refers to the first (second) zero of J_1 . Both positive peaks of the first perturbation which were seen to correspond to the first two zeros of J_0 have disappeared in the total DOS. A careful look at the dispersion relations in Fig. 7 reveals that there is an excellent correspondence between the resonance peaks in the DOS and the plasmon dispersion for a given ζ , except for the lowest extended mode in the radiative region (towards the left of the light line) that could be reproduced neither in the local nor in the total DOS. This is not surprising, however, given the distinct nature of searching the zeros of the determinant for the dispersion spectrum in Fig. 7. We believe that in some better way of searching the zeros of the complex transcendental function for this purpose, such mode(s) may either disappear once and for all or will not yield a good correspondence with the resonance in the DOS.

Figure 10 illustrates the plasmon dispersion for the GaAs plasma shell asymmetrically bounded by unidentical dielectrics ($\text{Ga}_{1-x}\text{Al}_x\text{As}$ in the inner cylinder and SiO_2 in the outer

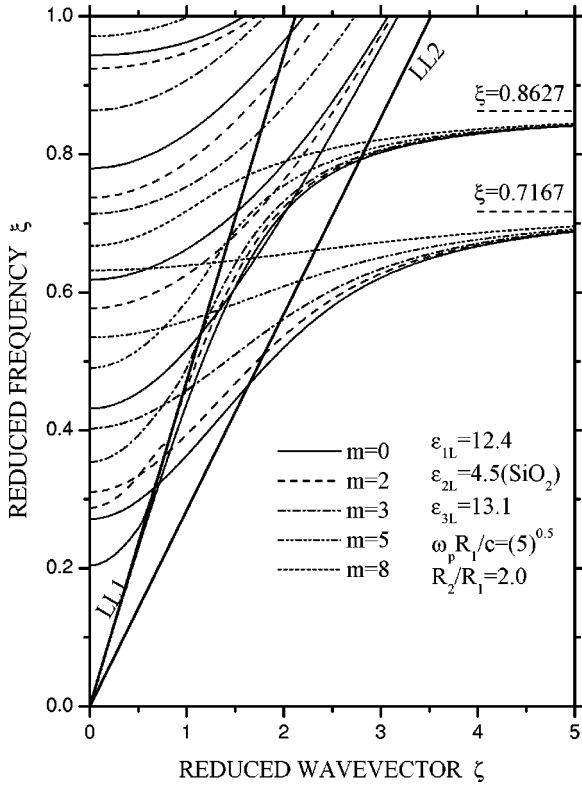


FIG. 10. Plasmon dispersion in a GaAs plasma ($\epsilon_{3L}=13.1$) shell sandwiched between unidentical $\text{Ga}_{1-x}\text{Al}_x\text{As}$ ($\epsilon_{1L}=12.4$) and SiO_2 ($\epsilon_{2L}=4.5$) dielectrics. There are five groups of curves for five different values of m . The solid straight line labeled LL1 (LL2) refers to the light line in the SiO_2 ($\text{Ga}_{1-x}\text{Al}_x\text{As}$). The dashed horizontal line labeled $\xi=0.7167$ ($\xi=0.8627$) indicates the asymptotic frequency for the interface R_1 (R_2). The parameters used in the computation are as listed in the picture.

semi-infinite medium). For other parameters involved in the computation, we consider $\omega_p R_1/c = \sqrt{5}$ and $R_2/R_1 = 2.0$. The solid, dashed, dash-dotted, dash-dot-dotted, and dotted curves represent, respectively, the cases for $m=0, 2, 3, 5$ and 8 . The two solid straight lines marked as LL1 and LL2 refer to the light lines in the dielectric media SiO_2 and $\text{Ga}_{1-x}\text{Al}_x\text{As}$, respectively. The two dashed horizontal lines labeled as $\xi=0.7167$ and $\xi=0.8627$ stand for the asymptotic frequencies for the plasmon polaritons propagating at the interface R_1 and R_2 , respectively. Unlike the symmetric case (see Fig. 7), the two plasma modes at a large propagation vector ζ approach the different asymptotic limits. Comparing Fig. 10 with Fig. 7 reveals that the asymmetric case yields a relatively richer spectrum at least for the radiative modes for a given m . Interesting, but not unexpected, is the fact that only the lowest pair of modes for every m crosses the rightmost lightline and attains the character of a pure plasmon-polariton before becoming asymptotic to the respective frequencies. It is also noteworthy that each pair of such modes (for a given m) observes an intersection between its branches in the radiative region towards the left of the leftmost light line. This remains true at least for the lower values of m (see, e.g., $m=0, 2, 3$, and 5). After such an intersection, originally lower (upper) branch becomes asymptotic to the upper (lower) frequency at large ζ .

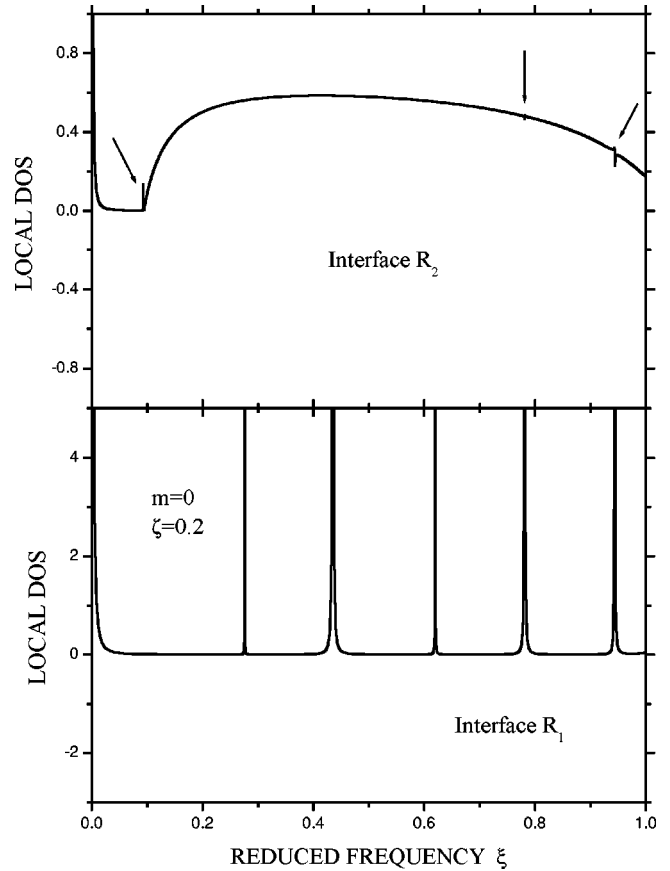


FIG. 11. Local density of states at the interface R_1 (R_2) in the lower (upper) panel for $m=0$ and $\zeta=0.2$. We call attention to the smaller DOS resonances, indicated by arrows, corresponding to the interface R_2 . The rest of the parameters used are the same as in Fig. 10.

Figure 11 depicts the local density of states at interface R_1 (R_2) in the lower (upper) panel for $m=0$ and $\zeta=0.2$. Other parameters are the same as those used in Fig. 10. One can see five clear resonances lying at $\xi=0.2759, 0.4351, 0.6199, 0.7815$, and 0.9441 at interface R_1 , whereas the interface R_2 observes only three at $\xi=0.09284, 0.7815$, and 0.9441 . Thus the two interfaces share only the two highest resonances in the local DOS and with a difference of magnitude. Again, the two interfaces pose different preferences, and that makes more sense here because of the asymmetric configuration. Note that only the lowest resonance at interface R_2 belongs to the confined plasmon mode; the rest of the higher ones correspond to the radiative modes.

Figure 12 shows the total density of states for the same system as discussed in Figs. 10 and 11 for $m=0$ and $\zeta=0.2$. We find that there are six well defined positive resonances lying at the same frequencies as those specifying the resonance peaks in the local DOS (summing up all the peaks at both interfaces in Fig. 11). In addition, there are three negative peaks occurring at $\xi=0.09428, 0.4899$, and 0.8928 , which have no physical significance. While the first one comes from the second perturbation, the pair of the second and third negative peaks emerges from the first perturbarion (i.e., $|\tilde{g}_1^{-1}|=0$); their positions in frequency correspond to

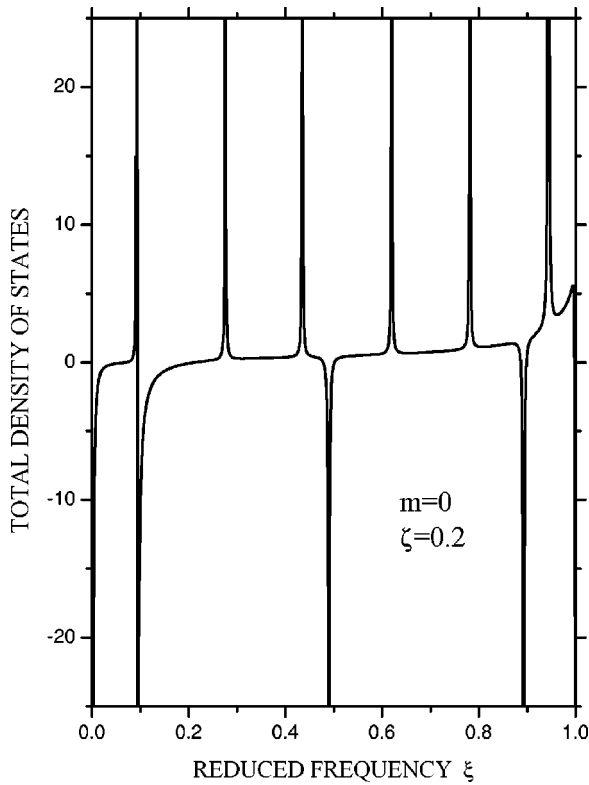


FIG. 12. Total density of states for $m=0$ and $\zeta=0.2$. The rest of the parameters used are the same as in Fig. 10. While the lowest negative peak emerges from the second perturbation, the two higher peaks come from the first perturbation. Such negative peaks have no physical significance.

the first three zeros of the Bessel function J_1 . The two positive resonances observed in the first perturbation, which correspond to the first two zeros of J_0 , have disappeared from the total DOS. It is found that all the six resonances in the DOS reproduce exactly the frequencies of the plasmon modes of Fig. 10 at the given ζ , with the exception for the lowest radiative mode above the left light line. However, this mode is found to have the same story as the corresponding one in Fig. 7 and hence our comments made in relation to Fig. 9 remain valid.

Finally, we take up the case of a dielectric ($\text{Ga}_{1-x}\text{Al}_x\text{As}$) shell symmetrically bounded by two identical GaAs plasmas for $\omega_p R_1/c = \sqrt{2}$ and $R_2/R_1 = 2.5$. The results for the plasmon dispersion in terms of dimensionless frequency (ξ) and wave vector (ζ) are plotted in Fig. 13. The solid, dashed, dash-dotted, dash-dot-dotted, and dotted curves correspond to $m=0, 2, 3, 5,$ and 8 , respectively. The solid straight line marked as LL refers to the light-line in the dielectric shell and the dashed horizontal line labeled as $\xi=0.7167$ indicates the asymptotic frequency for the plasmon polariton at the large value of ζ . One can easily notice that while the number of the modes in the nonradiative region is still two, the number of radiative modes (towards the left of the light line) is larger for any m as compared to that in Figs. 7 and 10. Also, it is evident that no such nasty mode (as the lowest radiative mode encountered in Figs. 7 and 10) is seen to be emerging in this case.

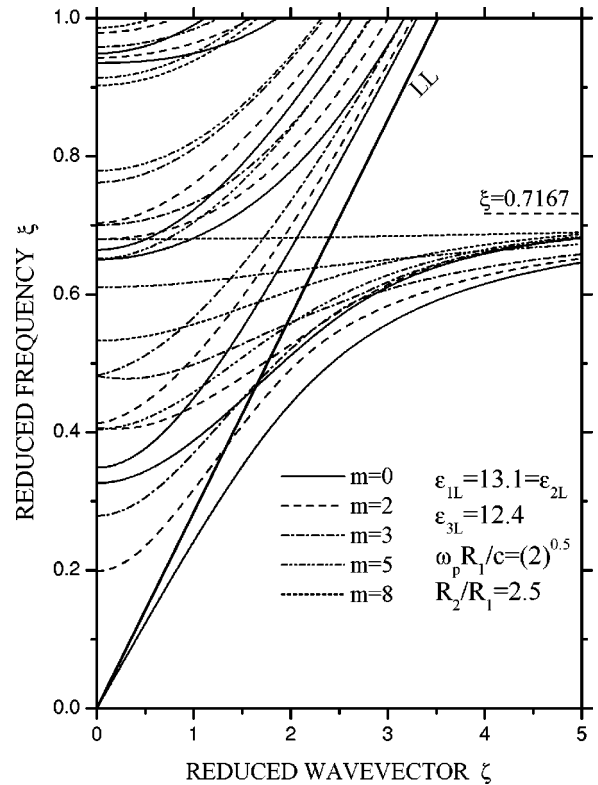


FIG. 13. Plasmon dispersion in a $\text{Ga}_{1-x}\text{Al}_x\text{As}$ dielectric ($\epsilon_{3L} = 12.4$) shell sandwiched between identical GaAs plasmas ($\epsilon_{1L} = 13.1 = \epsilon_{2L}$). There are five groups of curves for five different values of m . The solid straight line labeled as LL refers to the light line in the $\text{Ga}_{1-x}\text{Al}_x\text{As}$ dielectric. The parameters used in the computation are as listed in the picture.

Figure 14 illustrates the local density of states at interface R_1 (R_2) in the lower (upper) panel for $m=0$ and $\zeta=0.5$. It is found that there are seven well-defined resonances lying at $\xi=0.1229, 0.3433, 0.3765, 0.6582, 0.6793, 0.9380,$ and 0.9594 shared by both interfaces, of course with a difference of magnitude. In that sense, this case is much different than the previous ones of plasma shell between two dielectrics (see, e.g., Figs. 8 and 11). Again, it is only the lowest resonance that substantiates the confined plasmon mode below the light line, the rest correspond to the radiative modes for this value of ζ .

Figure 15 shows the total density of states for the same system as investigated in Figs. 13 and 14 for $m=0$ and $\zeta=0.5$. We observe that there are seven well-defined positive resonances located at the same frequencies as those specifying the similar resonance peaks in the local DOS (see Fig. 14). Moreover, two negative resonances are seen to emerge at $\xi=0.4557$ and 0.8598 . These negative peaks are a consequence of the third perturbation alone that produces three positive peaks lying at $\xi=0.14199 \Rightarrow \beta_3=0, 0.4398,$ and 0.8507 and the two negative peaks as mentioned above. While all three positive peaks disappear from the total DOS, the two negative peaks survive. The surviving negative peaks are seen to be the exact solutions of $|\tilde{g}_3^{-1}|=0$. The case studied in Figs. 13 – 15 for the coaxial cylindrical geometry

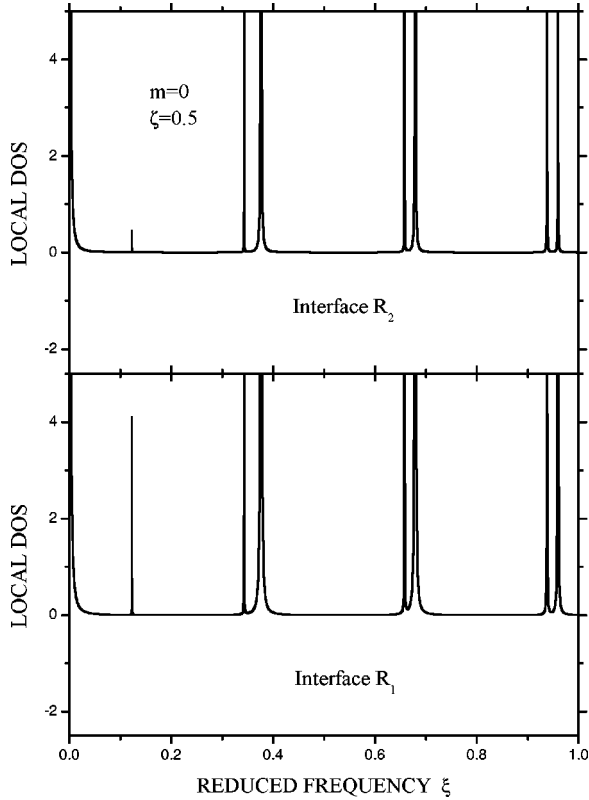


FIG. 14. Local density of states for $m=0$ and $\zeta=0.5$. The rest of the parameters used are the same as in Fig. 13.

seems to be the clearest one where there is no conflict at all between the DOS resonances and the plasmon dispersion.

We would like to stress that all the negative peaks in the variation of the total DOS showing up, for example, in Figs. 6, 9, 12, and 15 originate from the initial systems (or the so-called initial perturbations) comprising the resultant system. As noticed before, these are seen to be obtainable from the zeros of $|\tilde{g}_i^{-1}|$ (with $i \equiv 1, 2, \text{ or } 3$) wherever a dielectric medium is bounded by one (in the case of a single-interface system) or two (in the case of a double-interface system) black boxes. Since the black box does not represent a true physical system, though it is an essential ingredient of the theoretical scheme,⁴ these peaks have, in fact, no physical significance. However, they do exist with a negative sign in the TDOS, irrespective of the dimensionality, the size, and the shape of the system concerned.

It would not be out of place to mention that most of the modes covered by our results on the DOS correspond to those that fall in the radiative regime (i.e., towards the left of the leftmost light line in, for example, Figs. 5, 7, 10, and 13). The LDOSs in Figs. 6, 8, and 11 indicate that these modes are actually those of the $\text{Ga}_{1-x}\text{Al}_x\text{As}$ dielectric bounded by the GaAs plasma, confined on the dielectric side, and prohibited from propagation in the GaAs plasma. This is true despite the fact that depending on the thickness of the plasma shell the radiative modes in Figs. 8 and 11 can interact with the surrounding dielectric in the outer medium and hence may differ slightly from those in Fig. 6. Similarly, the modes in Fig. 14 are essentially those of the $\text{Ga}_{1-x}\text{Al}_x\text{As}$ shell that

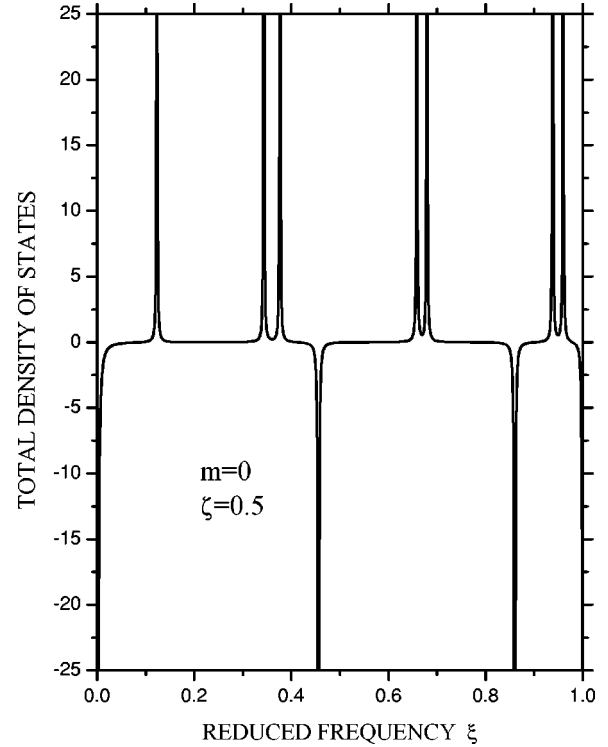


FIG. 15. Total density of states for $m=0$ and $\zeta=0.5$. The rest of the parameters used are the same as in Fig. 13. Both of the negative peaks emerge from the third perturbation alone and have no physical significance. The DOSs are shown in arbitrary units throughout.

are prohibited from propagation in the neighboring plasmas. This also explains why such peaks are so strong. The modes in the non-radiative regime (towards the right of the rightmost light line) tend to bear a different story. They originate from the dielectric-plasma heterointerface(s) and are plasmon-polariton-like.

V. CONCLUDING REMARKS

In summary, we investigated the plasmon dispersion and the density of states in the coaxial cylindrical geometries in the absence of any applied magnetic field. We derived the general dispersion relations using a Green-function theory in the framework of a IRT,⁴ which has now found widespread use to study numerous excitations in various composite systems.⁵⁻⁹ In doing so, we not only clarify some basic notions in the use of the cylindrical geometries but also diagnose our general analytical results under special limits to reproduce some well-known results on 2D and 1D plasmon dispersion in quantum wells and quantum wires. We have also successfully attempted to substantiate our results on plasmon dispersion through the computation of the local and total density of states. While we considered the effect of retardation, the absorption was neglected throughout, except for a small imaginary part needed to be added to the frequencies for the purpose of computing the DOS. The present methodology for coaxial cylindrical geometries is expected to prove to be a powerful theoretical framework for studying, for example, the intrasubband plasmons in the multi-walled carbon nanotubes.

We believe that an experimental observation of the radiative as well as non-radiative plasmon modes in such coaxial cylindrical geometries would be of great interest. Such experiments could possibly involve the well known attenuated total reflection, scattering of high energy electrons, or even Raman spectroscopy. Electron energy loss spectroscopy is already becoming known as a powerful technique for studying the electronic structure, dielectric properties, and plasmon excitations in carbon nanotubes and carbon onions, for example. Our preference for plotting the numerical results in terms of the dimensionless frequency and propagation vector leaves free an option of choosing the plasma frequency lower or higher, just as the radii of the cylinders.

Several important problems remain open in the context of the present investigation. The issues which need to be considered, and which could give better insight into the problem, include the role of absorption, the effects of the spatial dispersion, the plasmons coupling to the optical phonons, effect of an applied electric field that may create the drifted charge

carriers and help study the instability mechanism, and most importantly the effect of an applied magnetic field in order to study, for example, the edge magnetoplasmons in the concentric cylindrical geometries, to name a few. Currently, we have been investigating the effects of an applied magnetic field in the Faraday geometry on the plasmon dispersion in such concentric cylindrical structures and the results will be reported shortly.

ACKNOWLEDGMENTS

One of us (M.S.K.) gratefully acknowledges the hospitality of the Sakaki Laboratory, Institute of Industrial Science, The University of Tokyo, Tokyo (Japan), during the sabbatical year 2002-2003. He would also like to express his sincere thanks to the Japan Society for the Promotion of Science (JSPS) for granting the long-term visiting fellowship (Grant Ref. 401331/ID # L02527).

¹For an extensive review of electronic, optical, and transport properties of systems of reduced dimensionality, such as quantum wells, wires, dots, and modulated 2D systems, see M. S. Kushwaha, *Surf. Sci. Rep.* **41**, 1 (2001).

²C. L. Foden, M. L. Leadbeater, and M. Pepper, *Phys. Rev. B* **52**, R8646 (1995).

³G. D. Banyard, C. R. Bennett, and M. Babiker, *Opt. Commun.* **207**, 195 (2002).

⁴L. Dobrzynski, *Surf. Sci. Rep.* **6**, 119 (1986); *Surf. Sci.* **300**, 1008 (1994).

⁵L. Dobrzynski and H. Puzkarski, *J. Phys.: Condens. Matter* **1**, 1239 (1989).

⁶M. S. Kushwaha and B. Djafari-Rouhani, *Phys. Rev. B* **43**, 9021 (1991); *Surf. Sci.* **244**, 336 (1991); **268**, 457 (1992).

⁷B. Djafari-Rouhani and L. Dobrzynski, *J. Phys.: Condens. Matter* **5**, 139 (1993).

⁸M. S. Kushwaha and B. Djafari-Rouhani, *Phys. Rev. B* **57**, 13 020 (1998).

⁹M. S. Kushwaha and B. Djafari-Rouhani, *Ann. Phys. (N.Y.)* **265**, 1 (1998).

¹⁰D. Pines and P. Nozieres, *The Theory of Quantum Liquids* (Benjamin, New York, 1966).

¹¹C. Dekker, *Phys. Today* **52** (5), 22 (1999).

¹²P. M. Morse and H. Feshbach, *Methods of Theoretical Physics* (McGraw-Hill, New York, 1953), Vol. II.

¹³M. Abramowitz and I. A. Stegun, *Handbook of Mathematical Functions* (Dover, New York, 1972).

¹⁴See, for example, R. Rupin, in *Electromagnetic Surface Modes*, edited by A. D. Boardman (Wiley, New York, 1982), p. 389, and references therein.

¹⁵J. Wang and J. P. Leburton, *Phys. Rev. B* **41**, 7846 (1990).

¹⁶Q. P. Li and S. Das Sarma, *Phys. Rev. B* **43**, 11 768 (1991).